REPORT DOCUMENTATION PAGE

1. REPORT DATE *(DD-MM-YYYY)*	2. REPORT TYPE	3. DATES COVERED *(From - To)*
08-06-2012	Final Performance Report	06/01/2009-05/31/2012

4. TITLE AND SUBTITLE

Design and Development of Novel Hierarchically Ordered Block Copolymer--Magnetoelectric Particle Nanocomposites

5a. CONTRACT NUMBER

5b. GRANT NUMBER
FA9550-09-1-0388

5c. PROGRAM ELEMENT NUMBER

6. AUTHOR(S)
Zhiqun Lin,[1,2] Mufit Akinc,[1] Xiaoli Tan,[1] and Nicola Bowler[1]

1. Department of Materials Science and Engineering, Iowa State University, Ames, IA 50011
2. School of Materials Science and Engineering, Georgia Institute of Technology, Atlanta, GA, 30332
   Phone: 404-385-4404;   Email: zhiqun.lin@mse.gatech.edu

5d. PROJECT NUMBER

5e. TASK NUMBER

5f. WORK UNIT NUMBER

7. PERFORMING ORGANIZATION NAME(S) AND ADDRESS(ES)
Iowa State University
1350 Beardshear Hall
Ames, IA 50011-2025

8. PERFORMING ORGANIZATION REPORT NUMBER

9. SPONSORING / MONITORING AGENCY NAME(S) AND ADDRESS(ES)
AFOSR/RSA
875 North Randolph Street
Suite 325, Room 3112
Arlington, VA 22203

10. SPONSOR/MONITOR'S ACRONYM(S)

11. SPONSOR/MONITOR'S REPORT NUMBER(S)
AFRL-OSR-VA-TR-2012-1174

12. DISTRIBUTION / AVAILABILITY STATEMENT
Distribution A: Approved for public release

13. SUPPLEMENTARY NOTES
The lead PI, Dr. Zhiqun Lin moved to Georgia Tech in August, 2011. The project was continued to be completed at both Iowa State and Georgia Tech by PIs.

14. ABSTRACT

Nanocomposite materials offer a vast design-space of potential material properties, depending on the properties of the constituents and their spatial arrangement. Nanocomposites of polymer/nanoparticle, formed by incorporating nanoparticles into a polymer matrix, have received a great deal of research interest from the scientific community because of the potential performance enhancement relative to either of the non-hybrid constituents. This 36 month effort has led to three major accomplishments: (1) synthesized novel nanostructured composites (i.e., nanocomposites incorporating ferroelectric nanoparticles and SPIONs intimately and permanently capped with polymers on the surface); (2) characterized the nanocomposites developed under 1 by measuring their dielectric and magnetic properties as a function of temperature and frequency; and (3) modeled the dielectric and magnetic properties of the nanocomposites in terms of the electromagnetic parameters and spatial arrangement of the constituents in order to facilitate design of materials with specified properties. The potential benefits of employing ferroelectric and magnetic materials in nanocomposites are manifested not only in the number of applications (e.g., sensors, spintronics devices, capacitors, actuators, transducers, etc.) that are anticipated to fill a critical need in future military, but also in the gaining of fundamental knowledge and expertise on the structure-property relationships in these novel nanostructured materials.

15. SUBJECT TERMS

16. SECURITY CLASSIFICATION OF:			17. LIMITATION OF ABSTRACT	18. NUMBER OF PAGES	19a. NAME OF RESPONSIBLE PERSON
a. REPORT	b. ABSTRACT	c. THIS PAGE			19b. TELEPHONE NUMBER *(include area code)*

Design and Development of Novel Hierarchically Ordered Block Copolymer–Magnetoelectric Particle Nanocomposites

Zhiqun Lin

School of Materials Science and Engineering, Georgia Institute of Technology, Atlanta, GA 30332

E-mail: zhiqun.lin@mse.gatech.edu

Over the past three years, we have made very good progress on the project. The key results are summarized as follows.

1. A general and robust strategy for monodisperse nanocrystals by capitalizing on amphiphilic unimolecular star-like block copolymers as nanoreactors

Nanocrystals exhibit a wide range of unique properties (e.g., electrical, optical, and optoelectronic) that depend sensitively on their size and shape, and are of both fundamental and practical interest. Breakthrough strategies that will facilitate the design and synthesis of a large diversity of nanocrystals with different properties and controllable size and shape in a simple and convenient manner are of key importance in revolutionarily advancing the use of nanocrystals for a myriad of applications in lightweight structural materials, optics, electronics, photonics, optoelctronics, magnetic technologies, sensory materials and devices, catalysis, drug delivery, biotechnology, and among other emerging fields.[1-3] Herein, we report a general strategy for crafting a large variety of functional nanocrystals with precisely controlled dimensions (i.e., plain, core/shell, and hollow nanoparticles) by capitalizing on a new class of amphiphilic *unimolecular* star-like block copolymers as nanoreactors. This strategy is effective and able to produce highly monodisperse nanoparticles, including metallic, ferroelectric, magnetic, luminescent, semiconductor, and their core/shell nanoparticles, which represent a few examples of the kind of nanoparticles that can be produced using this technique. We believe these nanoparticles can be utilized as building blocks or additives for bottom-up nanofabrication to develop low-cost nanoscale materials and devices with integrated functionalities enabled by the properties of individual nanoparticles and their proper spatial arrangement, and can also serve as model systems for fundamental research in self-assembly, phase behavior and crystallization kinetics of nanoparticles.[4-6]

Introduction

Among a variety of techniques such as vapor condensation and solid-state processes for producing nanoparticles (NPs), colloidal synthesis[7, 8] represents a simple chemical synthesis involving the formation of high-quality NPs in a liquid medium composed of various reactants from a broad range of materials. In recent years, many approaches, including organic solution phase synthesis,[2] thermolysis of organometallic precursors,[7] sol-gel process,[8] hydrothermal reaction,[9] liquid-solid-solution strategy,[3] polymer microgel reactor,[10] matrix-mediated synthesis in an ion exchange resin,[11] linear copolymer micelle templating,[12, 13] biomimetic synthesis using DNA or peptide templates,[14] etc. have been developed to synthesize inorganic NPs. Most of these approaches often require certain stringent experimental conditions and are difficult to generalize. Some approaches cannot afford the synthesis of NPs with tunable size, while the others yield NPs with non-uniform size and shape. For example, an elegant route to a wide

diversity of NPs based on a phase transfer and separation at the liquid/solid/solution interfaces in autoclave has been developed;[3] notably, complex core/shell and hollow NPs cannot be produced using this approach. Recently, functional nanocrystals (e.g., Au, TiO_2, $PbTiO_3$, etc.) have been synthesized by utilizing linear amphiphilic block copolymer micelles as template coupled with sol-gel chemistry;[15] however, these conventional linear polymeric micelles represent thermodynamic aggregates of amphiphilic molecules above their critical micelle concentration.[15] Thus, they are *dynamically* stable and their characteristics for a given system depend heavily on temperature and solvent properties. The shape of micelles may change upon varying experimental conditions, such as concentration, solvent, temperature, and pH.[16] Clearly, this approach is limited in scope. Only NPs that do not require high-temperature conversion from precursors can be prepared in the solution by reducing the solution containing precursors entrapped within block copolymer micelles.[15] On the other hand, dendrimers have been used as templates to prepare zerovalent metal NPs encapsulated within the dendrimer.[17] However, the synthesis of dendrimers requires relatively tedious multi-step reactions and purifications; their size, molecular weight and structure are difficult to be controlled. In addition, it is sterically difficult for precursors to enter the interior voids of dendrimer due to much higher branched density of the exterior, and thus the size and shape of NPs cannot be templated by dendrimers; only some nanoclusters with the size much smaller than dendrimer can be obtained.[18, 19]

In stark contrast to the approaches noted above, we exploited a series of amphiphilic multi-arm star-like block copolymers consisting of hydrophilic and hydrophobic blocks that are covalently linked to a small core as nanoreactors to craft monodisperse NPs with tunable sizes, different compositions and properties, and complex structures (e.g., core/shell and hollow). Importantly, these amphiphilic star-like block copolymers with well-controlled molecular architectures and molecular weights (i.e., poly(acrylic acid)-block-polystyrene (PAA-*b*-PS) diblock copolymer, poly(4-vinylpyridine)-block-poly(*tert*-butyl acrylate)-block-polystyrene (P4VP-*b*-P*t*BA-*b*-PS) and poly polystyrene-block-poly(*tert*-butyl acrylate)-block-polystyrene (PS-*b*-PAA-*b*-PS) triblock copolymers) form *unimolecular* micelles (i.e., composed of single copolymer molecule),[20, 21] which overcome the thermodynamic instability of conventional linear block copolymer micelles, thereby resulting in monodisperse, structurally stable spherical macromolecules.[16, 22]

Experimental

For plain NPs, 10 mg star-like PAA-*b*-PS template was dissolved in a 10 mL mixture of DMF and BA at room temperature (V_{DMF}/V_{BA} = 9:1), followed by the addition of an appropriate amount of precursors (e.g., $PbTi[OCH(CH_3)_2]_6$) that were selectively incorporated into inner PAA blocks. The molar ratio of acrylic acid (AA) units in the PAA block to precursor was 1:5 in order to maximize the loading of precursors into PAA domains. The mixture was then refluxed at elevated temperature for a period of time (e.g., 180°C for 2 h for $PbTiO_3$). For core/shell NPs, 10 mg star-like P4VP-*b*-P*t*BA-*b*-PS template was dissolved in a 10 mL mixture DMF and BA at room temperature (V_{DMF}/V_{BA} = 9:1). The core material was first formed via the encapsulation of its precursors (e.g., $FeCl_2 \cdot 4H_2O$:$FeCl_3 \cdot 6H_2O$:ammonium hydroxide = 1:1:1 by mole for Fe_3O_4) within the innermost P4VP regime, followed by reaction at certain temperature for a period of time (e.g., 50°C for 30min for Fe_3O_4). Likewise, the molar ratio of 4VP unit of P4VP block to precursors was 1:5. Subsequently, the P*t*BA blocks were hydrolyzed into PAA by annealing in phenyl ether at 200°C for 2 h. The shell materials was then formed by carrying out the reaction (e.g., refluxing at 180°C for 2h for $PbTiO_3$ using $PbTi[OCH(CH_3)_2]_6$ as precursor) with the use of PAA blocks as template while keeping other experimental conditions same. For hollow NPs, 10 mg star-like PS-*b*-PAA-*b*-PS template was dissolved in a 10 mL mixture DMF and BA at room temperature

(V_{DMF}/V_{BA} = 9:1). Similarly, the precursor (e.g., $HAuCl_4$) and reducer (such as ethanol, if applicable) were subsequently added into the template solution. After the reaction (e.g., at 60°C for 10h for Au), hollow NPs (e.g., Au) with PS blocks tethered on both sides of NP were obtained (see Supplementary Information for experimental details).

Results and Discussion

We firstly synthesized plain NPs using amphiphilic star-like PAA-*b*-PS diblock copolymer as template to demonstrate the effectiveness of our strategy in producing a wide spectrum of high-quality NPs. Three PAA-*b*-PS samples with different molecular weight (MW) and ratios of PAA to PS blocks were synthesized via sequential atom transfer radical polymerization (ATRP), in which β-cyclodextrin (β-CD)-based star-like 21-Br-β-CD with 21 initiating sites was used as macroinitiator[16] (**Fig. 1a**, Table S1, and Supporting Material Section I). One important characteristic of star-like block copolymers as *unimolecular* micelles is their size, which is defined as the hydrodynamic diameter, D_h, in a particular solvent. The D_h values of synthesized star-like PAA-*b*-PS in dimethylformamide (DMF) were measured by dynamic light scattering (DLS) (Table S4, and Supporting Online Material Section II).

The inner PAA block in the *unimolecular* micelles is highly hydrophilic and imparts the preferential incorporation of precursors in the space occupied by 21 PAA blocks via a strong coordination bonding between the metal moiety of precursors and functional groups of PAA (i.e., -COOH);[23] while there was no such coordination with the outer hydrophobic PS blocks. Subsequent condensation and hydrolysis of appropriate precursors in the mixed solvents of DMF and benzyl alcohol (BA) formed desired NPs with PAA blocks encapsulated inside (see Supporting Material Section VI for the proposed formation mechanism), while the surface of NPs was *intimately* and *permanently* connected with hydrophobic PS blocks (**Fig. 1a**).

The synthesis of ferroelectric $PbTiO_3$ NPs was used as a typical example to illustrate the protocol depicted in **Fig. 1a**. The diameter of $PbTiO_3$ NPs can be readily controlled by varying the chain length of PAA block during ATRP of *tert*-butyl acrylate (*t*BA), which was further hydrolyzed into PAA (Table S4). Three $PbTiO_3$ NPs with different diameters (i.e., D = 5.7±0.2 nm, 9.8±0.4 nm, and 16.1±0.6 nm (**Fig. 2a**)) were achieved by utilizing three different star-like PAA-*b*-PS as nanoreactors (Tables S1 and S4). The representative high resolution TEM (HRTEM) characterization on 9.8±0.4-nm $PbTiO_3$ NPs revealed that they possessed continuous crystal lattice with a lattice spacing of 2.76Å, corresponding to the (110) crystalline plane of tetragonal phase of $PbTiO_3$ (i.e., forming single crystal structures) (**Fig. 2a,** lower left; and Fig. S25)**.** The formation of single crystals may be qualitatively understood as follows. The volume fraction of PAA blocks encapsulated in the 9.8±0.4-nm NP was approximately only 13.8% based on the thermogravimetric analysis (TGA) measurement (Supporting Material Section VIII). As the reaction was performed at 180°C, and lower than the degradation temperature of polymer templates (T_d = 210°C according to TGA; Supporting Material Section VIII), the chain segments of PAA-*b*-PS (e.g., AA units) may either substitute the atoms on specific crystalline lattice of NPs and became part of lattice structure or intercalate the lattices, thereby resulting in single crystalline NPs regardless of the presence of PAA chains. Similar phenomenon has been broadly observed in the organic molecule/inorganic crystal systems.[24-26] Nonetheless, this will be the subject of future study.

Quite intriguingly, the volume ratio of DMF to BA in the mixed solvents exerted a profound influence on the uniformity of the resulting NPs. Tailoring the solubility of polymer chains in
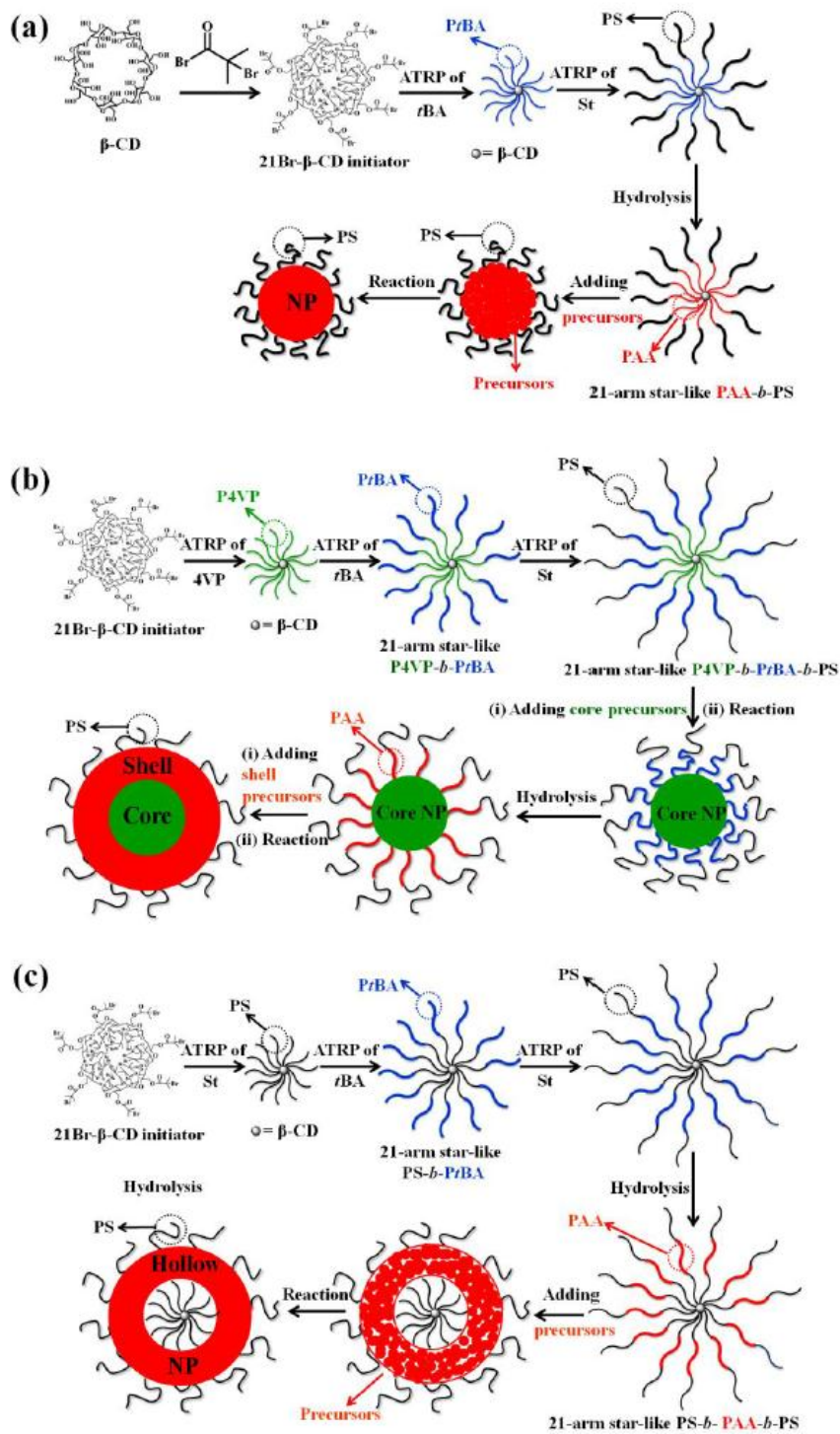
Figure 1. Schematic representation of synthetic strategies for nanoparticles (NPs) by capitalizing on amphiphilic star-like block copolymers as nanoreactors. (a) Formation of plain NPs, (b) formation of core/shell NPs, and (c) formation of hollow NPs.

amphiphilic block copolymers using mixed selective solvents can facilitate the encapsulation of inorganic precursors in a better defined spherical space composed of inner hydrophilic PAA blocks, from which NPs nucleate and grow, and represents the key to our method (**Fig. 2c**). Obviously, when DMF was the only solvent used, $PbTiO_3$ NPs possessed relatively irregular shape (DMF:BA = 10:0 by volume) (**Fig. 2b**; left). In the 9/1 DMF/BA solvents, $PbTiO_3$ NPs with the best uniformity were yielded (**Fig. 2b**; center). As more BA was added (i.e., DMF : BA = 5 : 5), the regularity of NPs decreased again (**Fig. 2b**; right).

The mechanism of the growth of *monodisperse* NPs can be rationalized considering the solubility of each block in DMF and BA. DMF is a good solvent for PAA and PS blocks. The star-like PAA-*b*-PS can be readily dissolved in DMF, forming *unimolecular* micelle (**Fig. 2c**; upper left). Upon the addition of BA, which dissolves PAA relatively much better than PS (i.e., a solvent for PAA but a non-solvent for PS), the outer PS blocks collapsed due to unfavorable interaction between PS and BA while the inner PAA blocks retained coil-like conformation. At the 9/1 DMF/BA, a transformation from fully expanded chain conformation in pure DMF (**Fig. 2c**; upper left) into more compact and structurally stable spherical macromolecule occurred (**Fig. 2c**; center left). The density of inner PAA blocks (i.e., the number of chains per volume) was slightly increased, representing in the slight shrinkage in their chain length as evidenced by comparing the TEM (**Fig. 2a**) with DLS measurements (Table S4), for example, 5.7±0.2-nm by TEM as compared to 7±0.5-nm D_h of PAA by DLS (Table S4). At the same time, the loading of precursors into this well-defined regime composed of PAA chains was increased, thereby yielding NPs with markedly improved quality (**Fig. 2a;** and **Fig. 2b**, center right). However, with the addition of more BA (i.e., DMF/BA = 5:5), a significant collapse of outer PS chains was encountered (**Fig. 2c**; lower left), making it difficult for precursors to enter the PAA regime, and thus forming non-uniform NPs (**Fig. 2b**; right).

Remarkably, the strategy of star-like block copolymer nanoreactor for the NP synthesis is quite general. It can be readily extended to produce a large variety of NPs with good uniformity (the size distribution lies within 5% of the average size) and solubility, including noble metal (Au and Ag), ferroelectric ($BaTiO_3$ and $PbTiO_3$ (Fig. S30)), magnetic (Fe_3O_4, exhibiting superparamagnetic properties (Fig. S9)), semiconductor (luminescent CdSe, *n*-type TiO_2 (Fig. S31), *n*-type ZnO (Fig. S32), *p*-type Cu_2O) NPs as shown in the representative TEM images (**Fig. 3**) and digital images (Fig. S2). The energy dispersive spectroscopy (EDS) microanalysis and X-ray diffraction (XRD) measurements substantiated the success in synthesizing these NPs (Supporting Material Section IV). The reaction was performed at different temperature over a different period of time for specific materials (Supporting Material Section V). These functional NPs are *intrinsically* linked to outer hydrophobic PS blocks, imparting the solubility in nonpolar solvents. The solutions were homogeneous and stable for months (i.e., 18 months); no precipitation was observed.

Of particular interest is that our strategy for highly crystalline NPs is remarkably versatile. In addition to plain NPs, we also synthesized core/shell NPs. Core/shell nanostructures are conventionally obtained by dissimilar materials epitaxy, which requires moderate lattice mismatches (<2%) between the two different materials in order to obtain high-quality core/shell heterostructures, which would otherwise be difficult to obtain.[27, 28] For example, the formation of crystalline semiconductor on metal structures remained challenging by epitaxial growth due to their differences in crystal structure, bonding, and materials properties.[27, 28]
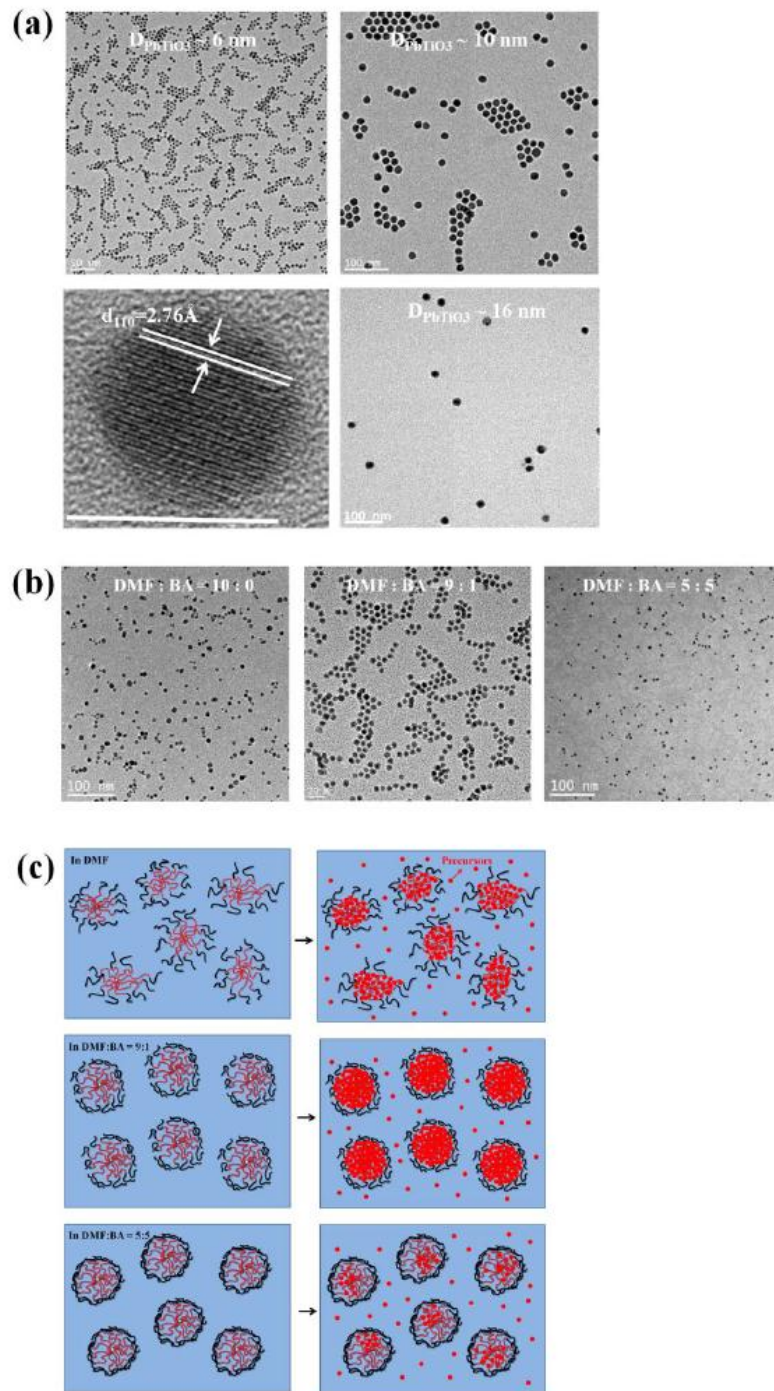
Figure 2. (a) TEM images of three PbTiO$_3$ NPs with different diameters (D = 5.7±0.2nm, 9.8±0.5nm, and 16.1±0.6nm) prepared by employing three star-like PAA-*b*-PS with different molecular weight of PAA block as nanoreactors, respectively (Table S1). HRTEM image of 9.8±0.5-nm NPs is shown on the lower left panel, suggesting the formation of single crystal structure; scale bar = 10nm. (b) TEM images of PbTiO$_3$ NPs formed in the mixed solvents of DMF and BA at different volume ratios (V$_{DMF}$: V$_{BA}$ = 10:0, 9:1, and 5:5, respectively). (c) The proposed mechanism for the growth of *uniform* and *non-uniform* NPs in DMF and BA.

As outlined in **Fig. 1b**, our general strategy of capitalizing on a new class of star-like triblock copolymer as nanoreactor renders the creation of a wide diversity of core/shell NPs with well-controlled size of core and shell materials, and different compositions and properties, including but not limited to metal/semiconductor or semiconductor/metal (e.g., Au/CdSe or CdSe/Au), metal/metal oxide or metal oxide/metal (i.e., Au/Fe_3O_4 or Fe_3O_4/Au), and dissimilar metal oxide core/shell NPs (i.e., magnetic/ferroelectric Fe_3O_4/$PbTiO_3$, ferroelectric/magnetic $PbTiO_3$/Fe_3O_4, Fe_3O_4/$BaTiO_3$, and $BaTiO_3$/Fe_3O_4) (Fig. S12-S16). As such, it dispenses with the need for epitaxial growth for promising applications in nanoscale waveguides, sensors, spintronics, bioimaging and biolabeling, etc.

First, similar to star-like PAA-*b*-PS, star-like poly(4-vinylpyridine)-block-poly(*tert*-butyl acrylate)-block-polystyrene (P4VP-*b*-P*t*BA-*b*-PS) triblock copolymers (**Fig. 1b**) were synthesized by sequential ATRP of 4-vinylpyridine, *tert*-butyl acrylate, and styrene (Supporting Material Section I). Two P4VP-*b*-P*t*BA-*b*-PS samples with different molecular weight and the block ratios were prepared. Similarly, the growth of core/shell NPs was based on the coordination reaction between functional blocks in star-like triblock copolymer and respective precursors (**Fig. 1b**). The size of core and shell materials can be readily tuned by altering the length of the first P4VP block and the second P*t*BA block (hydrolyzed into PAA later), respectively. More importantly, because the growth of shell was completely templated by functional second block of triblock copolymer, the shell lattice structure can be independent of the core material,[27] thus circumventing the limitations imposed by epitaxial growth.

We chose the synthesis of magnetic/ferroelectric Fe_3O_4/$PbTiO_3$ NPs as an example. The Fe_3O_4 core was first formed via the encapsulation of its precursors within the innermost P4VP regime through the selective coordination interaction between the N atoms of P4VP blocks (**Fig. 1b**) and the metal moieties of precursors (Fig. S33).[15] The diameter of Fe_3O_4 core was about 6.1±0.3nm (**Fig. 4a**). Subsequently, the P*t*BA blocks situated on the surface of Fe_3O_4 core were hydrolyzed into PAA (Supporting Material Section VII). The $PbTiO_3$ shell was then formed by using PAA blocks as template (Fig. S34). **Figure 4b** shows the TEM images of Fe_3O_4/$PbTiO_3$ NPs with uniform size and narrow size distribution, where the crystalline $PbTiO_3$ shell was clearly evident in HRTEM image (**Fig. 4b**; lower left; 3.1±0.3nm thick). The crystal structures of Fe_3O_4 and $PbTiO_3$ were further corroborated by the EDS and XRD measurements (Fig. S15). Strikingly, despite more than 40% lattice mismatch between Fe_3O_4 and $PbTiO_3$,[27] the Fe_3O_4/$PbTiO_3$ NPs were successfully synthesized by exploiting our robust star-like triblock copolymer template strategy. Other core/shell NPs can also be produced as long as appropriate precursors are identified (e.g., Fe_3O_4/Au in Fig. S27, S33 and S35, and Au/CdSe in Fig. S28).

Quite interestingly, amphiphilic star-like triblock copolymers can also be employed to structure-direct precursors into hollow monodisperse NPs by selectively sequestering precursors in the intermediate block and growing into NPs. Hollow nobel metal NPs are the subject of intense research for use in bioimaging, photothermal therapy and drug delivery.[29] We prepared hollow Au NPs by employing star-like poly(styrene)-block-poly(acrylic acid)-block-polystyrene (PS-*b*-PAA-*b*-PS) triblock copolymer templates (Table S3; Supporting Material Section I). The Au precursors were exclusively confined in the intermediate PAA regime (**Fig. 1c**), and ultimately yielded hollow Au NPs with hydrophobic PS blocks *intimately* tethered on both inside and outside the Au surface. Notably, this class of intriguing NPs may be regarded as organic/inorganic core/shell NPs (e.g., PS core and Au shell).
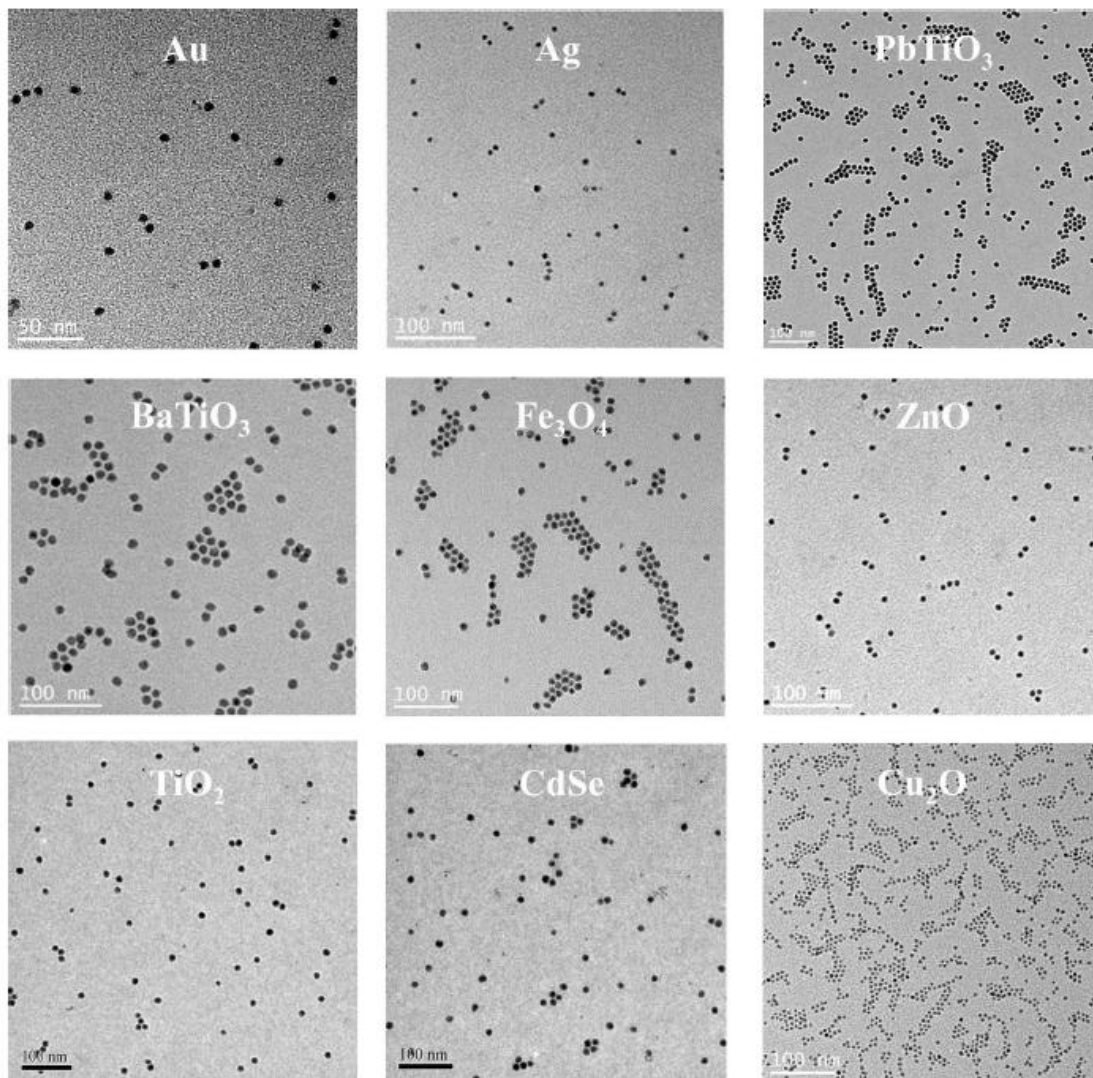
Figure 3. Representative TEM images of a large variety of NPs synthesized by utilizing star-like PAA-*b*-PS templates (i.e., sample-A and sample-B in Table S1). The diameters of NPs are: noble metals D_{Au} = 5.6±0.6nm and D_{Ag} = 6.1±0.3nm; ferroelectrics D_{PbTiO3} = 9.7±0.4nm and D_{BaTiO3} = 10.4±0.3nm; magnetic D_{Fe3O4} = 10.1±0.5nm; and semiconductors D_{CdSe} = 9.9±0.3nm, D_{TiO2} = 10.2±0.2nm, D_{ZnO} = 6.3±0.6nm, and D_{Cu2O} = 6.4±0.2nm. All size distribution lies within 5% of the average size. The corresponding digital images are shown in Fig. S2.

It is not surprising that the TEM characterization clearly displayed that Au NPs were morphologically hollow, appearing bright in the center of NPs (**Fig. 4c**). Highly crystalline nature of these hollow NPs was manifested in the HRTEM image, where the crystalline lattice was partially appeared in the center; this can be attributed to the imaging effect due to the presence of crystalline Au shell on the top of hollow core. Moreover, the composition and elemental distribution of hollow structures mapped by EDS and XRD measurements further proved the successful formation of hollow Au NPs (e.g., Fig. S17). The size of hollow NPs can be conveniently controlled by varying the length of innermost PS block and intermediate P*t*BA block during ATRP of styrene (St) and *t*BA, and thus allowing for the production of a variety of
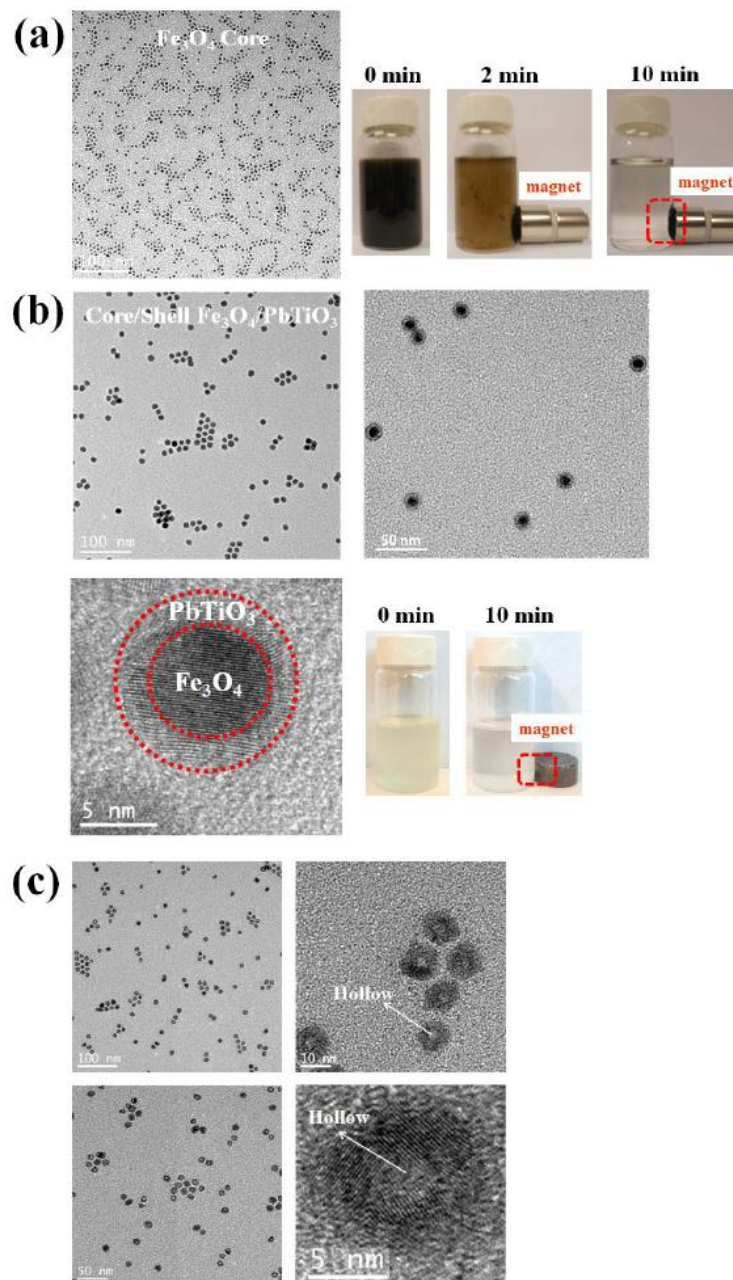
8

Figure 4. (a-b) TEM images of (a) Fe_3O_4 core (D_{Fe3O4} = 6.1±0.3nm) and (b) $Fe_3O_4/PbTiO_3$ core/shell NPs at different magnifications (the $PbTiO_3$ shell thickness = 3.1±0.3nm), in which Fe_3O_4 appeared dark. HRTEM clearly showed the crystalline lattices of Fe_3O_4 core and $PbTiO_3$ shell with the red dash circles used to guide for the eyes. The magnetic properties in $Fe_3O_4/PbTiO_3$ NPs were retained as clearly evidenced in the digital images of NP toluene solution in response to the magnet bars; with which the NPs were deposited on the wall of vials (marked with red boxes). For Fe_3O_4 core materials only, the toluene solution appeared dark at high concentration, originating from Fe_3O_4 ((a), right); for $Fe_3O_4/PbTiO_3$ core/shell NPs, the toluene solution appeared white, originating from $PbTiO_3$ shell ((b), lower right). (c) TEM images of representative hollow Au NPs with uniform size distribution (the thickness of Au = 3.2±0.3nm, and the diameter of hollow core = 5.6±0.4nm).

hollow NPs with different size, for example, hollow noble metal Ag and semiconductor Cu_2O NPs (Fig. S29).

Our template strategy for monodisperse NPs with precisely controllable size, surface chemistry and modulated compositions (i.e., plain, core/shell and hollow) by capitalizing on amphiphilic *unimolecular* star-like block copolymers as nanoreactors is effective, robust and generalizable, and can occur for nearly all the transitional or main group metal ions and organometallics. In particular, it provides enormous opportunities for crafting desired core/shell NPs with emergent properties realized using dissimilar materials of precisely tunable ratio for exploring many fundamental nanoscale physics (such as exciton-plasmon resonant coupling as in CdSe/Au NPs[30]). All the NPs can serve as the building blocks for the bottom-up assembly for nanostructured materials and devices with desirable characteristics for use in energy and biomedical applications.[1-6] The NPs are *intimately* and *permanently* tethered with hydrophobic polymer chains, thereby rendering their solubility in nonpolar solvents and the long-term stability. We envision the extension of this strategy to water-soluble NPs by growing hydrophilic polymer (e.g., poly(ethylene glycol); PEG) as the outermost block. More complex NPs with multiple shells and precise compositional tailoring may also be made by using star-like tetrablock and pentablock copolymer templates (i.e., forming multifunctional core/shell1/shell2 and core/shell1/shell2/shell3 NPs). In addition to inorganic NPs, it is also viable to craft polymeric NPs of different dimensions by judiciously crosslinking the desirable blocks of these star-like block copolymer. For example, the selective crosslinking of intermediate blocks can lead to nanocapsules for potential applications in controlled release of drugs, inks, etc.[1, 29]

References
1. Langer, R. *Nature* **1998,** 392, (6679), 5.
2. Sun, Y. G.; Xia, Y. N. *Science* **2002,** 298, (5601), 2176.
3. Wang, X.; Zhuang, J.; Peng, Q.; Li, Y. *Nature* **2005,** 437, (7055), 121.
4. Tang, Z.; Zhang, Z.; Wang, Y.; Glotzer, S. C.; Kotov, N. A. *Science* **2006,** 314, (5797), 274.
5. Macfarlane, R. J.; Lee, B.; Jones, M. R.; Harris, N.; Schatz, G. C.; Mirkin, C. A. *Science* **2011,** 334, 204.
6. Chen, Q.; Whitmer, J. K.; Jiang, S.; Bae, S. C.; Luijten, E.; Granick, S. *Science* **2011,** 331, 199.
7. Peng, X. G.; Manna, L.; Yang, W. D.; Wickham, J.; Scher, E.; Kadavanich, A.; Alivisatos, A. P. *Nature* **2000,** 404, (6773), 59.
8. Yang, P.; Zhao, D.; Margolese, D. I.; Chmelka, B. F.; Stucky, G. D. *Nature* **1998,** 396, (6707), 152.
9. Liang, Y.; Li, Y.; Wang, H.; Zhou, J.; Wang, J.; Regier, T.; Dai, H. *Nat. Mater.* **2011,** 10, (10), 780.
10. Zhang, J.; Xu, S.; Kumacheva, E. *J. Am. Chem. Soc.* **2004,** 126, (25), 7908.
11. Ziolo, R. F.; Giannelis, E. P.; Weinstein, B. A.; O'Horo, M. P.; Ganguly, B. N.; Mehrotra, V.; Russell, M. W.; Huffman, D. R. *Science* **1992,** 257, (5067), 219.
12. Chai, J.; Wang, D.; Fan, X.; Buriak, J. M. *Nat. Nanotechnol.* **2007,** 2, (8), 500.
13. Nie, Z.; Petukhova, A.; Kumacheva, E. *Nat. Nanotechnol.* **2010,** 5, (1), 15.
14. Chiu, C.; Li, Y.; Ruan, L.; Ye, X.; Murray, C. B.; Huang, Y. *Nat. Chem.* **2011,** 3, 393.
15. Leong, W. L.; Lee, P. S.; Lohani, A.; Lam, Y. M.; Chen, T.; Zhang, S.; Dodabalapur, A.; G. Mhaisalkar, S. *Adv. Mater.* **2008,** 20, (12), 2325.
16. Pang, X.; Zhao, L.; Akinc, M.; Kim, J. K.; Lin, Z. *Macromolecules* **2011,** 44, (10), 3746.
17. Crooks, R. M.; Zhao, M.; Sun, L.; Chechik, V.; Yeung, L. K. *Accounts Chem. Res.* **2000,** 34, (3), 181.
18. Balogh, L.; Tomalia, D. A. *J. Am. Chem. Soc.* **1998,** 120, (29), 7355.

19.   Juttukonda, V.; Paddock, R. L.; Raymond, J. E.; Denomme, D.; Richardson, A. E.; Slusher, L. E.; Fahlman, B. D. *J. Am. Chem. Soc.* **2005,** 128, (2), 420.
20.   Liu, H.; Jiang, A.; Guo, J.; Uhrich, K. E. *J. Polym. Sci. Part A: Polym. Chem.* **1999,** 37, (6), 703.
21.   Newkome, G. R.; Moorefield, C. N.; Baker, G. R.; Saunders, M. J.; Grossman, S. H. *Angew. Chem. Int. Ed.* **1991,** 30, (9), 1178.
22.   Pang, X.; Zhao, L.; Feng, C.; Lin, Z. *Macromolecules* **2011**, 44, (10), 7176.
23.   Kidambi, S.; Dai, J.; Li, J.; Bruening, M. L. *J. Am. Chem. Soc.* **2004,** 126, (9), 2658.
24.   Kahr, B.; Gurney, R. W. *Chem. Rev.* **2001,** 101, (4), 893.
25.   Rohl, A. L.; Gay, D. H.; Davey, R. J.; Catlow, C. R. A. *J. Am. Chem. Soc.* **1996,** 118, (3), 642.
26.   Bullard, T.; Wustholz, K. L.; Bott, E. D.; Robertson, M.; Reid, P. J.; Kahr, B. *Crystal Growth & Design* **2009,** 9, (2), 982.
27.   Zhang, J.; Tang, Y.; Lee, K.; Ouyang, M. *Science* **2010,** 327, (5973), 1634.
28.   Palmstrom, C. J. *Annu. Rev. Mater. Sci.* **1995,** 25, 389.
29.   Im, S. H.; Jeong, U.; Xia, Y. *Nat. Mater.* **2005,** 4, (9), 671.
30.   Zhang, J.; Tang, Y.; Lee, K.; Ouyang, M. *Nature* **2010,** 466, (7302), 91.

2. High frequency dielectric properties of nanocomposites of PMMA mixed with PS capped BaTiO$_3$

A series of nanocomposites of PMMA/(BaTiO$_3$-PS) were prepared by utilizing PMMA as a dielectric host matrix and BaTiO$_3$-PS nanoparticles as fillers. The diameters of BaTiO$_3$-PS nanoparticles used in the study were 10 nm, 16 nm, and 25 nm, respectively. The dielectric properties of nanocomposites were measured over a microwave frequency range from 0.5 to 18GHz by Vector Network Analyzer (VNA). The permittivity of PMMA was determined to be 2.6. The permittivity of nanocomposites increased from 5 to 11 to 15 as the BaTiO$_3$ nanoparticle size decreased from 25 nm to 16 nm to 10 nm, respectively. Clearly, the nanoparticle size played an important role in dielectric properties of the resulting nanocomposites.

It is well known that in BaTiO$_3$ particles the ferroelectricity decreases as the particle size decreases and disappears below the critical size, which is about 10-20 nm.[1-4] To date, there has been little experimental evidence regarding the critical size.[5] In this regard, it is of particular interest in elucidating size-dependent properties of BaTiO$_3$ from fundamental and technological standpoints. In this study, a series of PMMA/(BaTiO$_3$-PS) nanocomposites with varied BaTiO$_3$ nanoparticle size of 10 nm, 16 nm, and 25 nm were prepared and the size-dependent high frequency dielectric constants of BaTiO$_3$ nanoparticles were explored.

Experimental

Sample preparation. Three PMMA/(BaTiO$_3$-PS) nanocomposites with BaTiO$_3$ nanoparticle size of 10 nm, 16 nm, and 25 nm were prepared, hereafter referred to as **PMMA/PS-BTO10, PMMA/PS-BTO16 and PMMA/PS-BTO25**, respectively, in which PMMA : BaTiO$_3$-PS = 1:4 by weight. Briefly, 0.075 g PMMA (MW = 50 K) and 0.3 g BaTiO$_3$-PS were dissolved in 10 mL dichloromethane (DCM). The mixture solution was stirred for 2 h, and then vacuumed to completely remove DCM at room temperature. Subsequently, the mixture powder was hot-pressed at 180^{0}C and possessed into a ring shape with inner and outer diameter of 3 mm and 7 mm, respectively.

Vector Network Analyzer (VNA) measurement. The permittivity of three nanocomposites was measured with an Anritsu 37347C Vector Network Analyzer incorporating an S-parameter test set and operating in the microwave frequency range from 0.5 GHz to 18 GHz. The complex permittivity was measured using coaxial transmission/reflection method for determining S-parameters. The conversion of S-parameters to complex permittivity was accomplished by applying well-known Nicholson-Ross-Weir algorithm.[6-8] After standard calibration of VNA, the validity of calibration was examined by measuring the permittivity

of Rexolite and comparing the measured permittivity with its known value. Finally, the permittivity measurements on PMMA and PMMA/PS-BTO samples were performed.

Results and Discussion

Permittivity of Rexolite from VNA measurement

Rexolite is known as a standard and widely used for permittivity measurement. It has a permittivity of 2.53. **Figure 5** shows the permittivity of Rexolite. It is clearly evident that the measured permittivity, $\varepsilon'_{Rexolite} = 2.52 \pm 0.4$ agreed well with the provided value of 2.53, suggesting the VNA system was well calibrated.
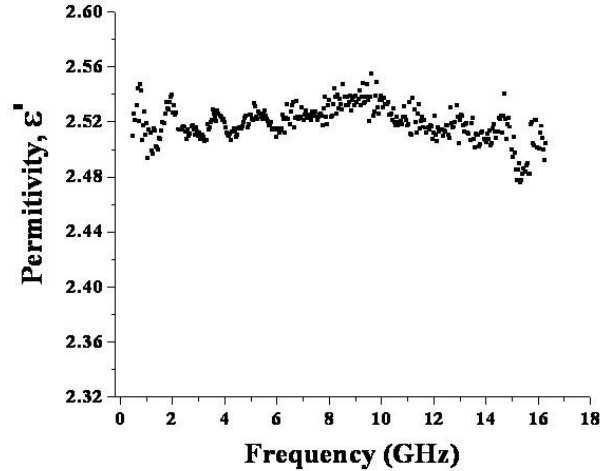

Figure 5. The permittivity of Rexolite in the microwave frequency range.

Dielectric properties of PMMA homopolymer and PMMA/PS-BTO nanocomposites

The real and imaginary parts of permittivity of PMMA sample are shown in **Figure 6**. Obviously, PMMA is dielectrically lossless and the dielectric constant, ε'_{PMMA} was approximately 2.6 over a wide frequency range from 1GHz to 18GHz. For the PMMA/PS-BTO nanocomposites, the real part increased from 5 to 11 to 15 with the nanoparticle size decreased from 25nm to 16nm to 10nm, respectively (**Figure 7a**). At the frequency around 9GHz, there was an apparent increase of the imaginary part of permittivity (**Figure 7b**).

The volume fractions of PMMA, f_{PMMA}, PS, f_{PS} and BaTiO$_3$, f_{BTO} in PMMA/PS-BTO nanocomposites are summarized in **Table 1**. The volume fraction of each component in nanocomposites was nearly the same despite different size BaTiO$_3$ nanoparticle used, indicating that the difference in permittivity of PMMA/PS-BTO nanocomposites (i.e., PMMA/PS-BTO10, PMMA/PS-BTO16 and PMMA/PS-BTO25) may be originated from the size effect of BaTiO$_3$ nanoparticles.
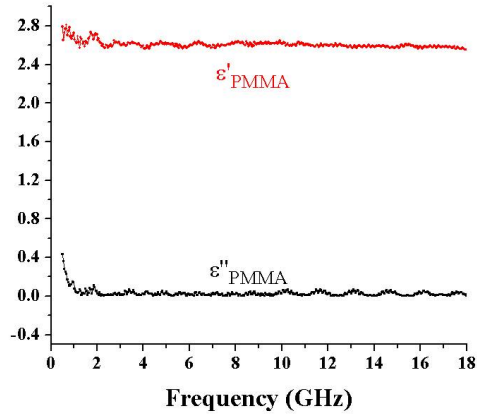
Figure 6. The permittivity of PMMA homopolymer. The real and imaginary parts of permittivity were shown in red and black lines, respectively.
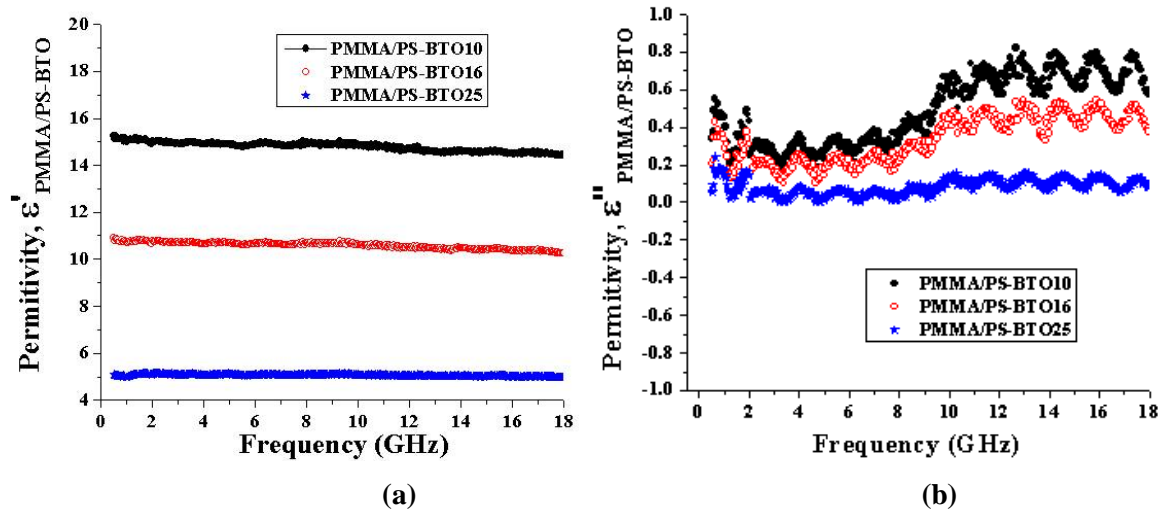

(a) **(b)**

Figure 7. The permittivity of PMMA/PS-BTO nanocomposites in which BaTiO$_3$ nanoparticle size were 10 nm (black solid circles), 16 nm (red open circles), and 25 nm (blue solid stars), respectively. (a) real part, ε'$_{PMMA/PS-BTO}$, and (b) imaginary part, ε''$_{PMMA/PS-BTO}$.

Table 1. Volume fractions of each component in PMMA/PS-BTO nanocomposites

Samples (at 1:4 ratio)	V(PMMA)/V(PS-BTO)	f_{PMMA}	f_{PS-BTO}	f_{PS}	f_{BTO}
PMMA/PS-BTO10	0.78971	0.44	0.56	0.25	0.30
PMMA/PS-BTO16	0.79807	0.44	0.56	0.25	0.31
PMMA/PS-BTO25	0.75739	0.43	0.57	0.28	0.29

13

Notably, small fluctuations observed in the permittivity measurements (Figures 8-10) may be rationalized as follows. First, during the calibration process, the broadband load, sliding load, short load, and open load were connected and disconnected to two GPC cables in order to complete the calibration, which may lead to a little change of the microwave pathway and eventually resulted in the system noise and error. As a result, after the calibration, no absolute value can be achieved when testing the permittivity of the standard, Rexolite. Thus, the small fluctuation in permittivity was due to the system error of VNA. Second, the PMMA/PS-BTO nanocomposites were fabricated into a ring-shaped sample. However, the sample may not be absolutely uniform. Moreover, there may be some defects in the sample (e.g., micron size holes). Consequently, when the microwave interacted with the sample, the response may also be not uniform.

References
1. G.Arlt, D. Hennings and G. De With. *J. Appl. Phys.* **58** (1985) 1619.
2. D. McCauley, R.E. Newnham and C.A. Randall. *J. Am. Ceram. Soc.* **81** (1998) 979.
3. M.R. Srinivasan, M.S. Multani, P. Ayyub and R. Vuayaraghavan. *Ferroelectrics* **51** (1983) 137.
4. A.J. Bell, A.J. Moulson and L.E. Cross. *Ferroelectrics* **54** (1984) 147.
5. Sotoshi WaDa, Hiroaki Yasuno and Takuya Hoshina. *Jpn. J. Appl. Phys.* **42** (2003) 6188.
6. A. M. Nicholson and G. F. Ross. *IEEE Trans. Instrmt. And Meas.*, Vol IM-4, No. 4, Nov. 1970, pp. 377-382.
7. J. Baker-Jarvis. *NIST Technical Note* 1341, July 1990.
8. W. B. Weir. *Proc. IEEE* **62**, 33{36 (1974).

3. Dielectric and ferroelectric properties of PS capped BaTiO$_3$

The dielectric and ferroelectric properties of PS capped BaTiO$_3$ nanoparticles (i.e., PS-BTO) were investigated. A series of samples with cubic phase of BaTiO$_3$ (denoted PS-BTOc) and tetragonal phase of BaTiO$_3$ with varied nanoparticle sizes (i.e., 10 nm (PS-BTO10) and 25 nm (PS-BTO25)) were hot-pressed. The dielectric properties of PS-BTO10 and PS-BTO25 were studied over a frequency range from 10^{-2} to 10^6 Hz with a temperature ranging from -40^{0}C to 160^{0}C by *Novocontrol* system. The temperature dependent dielectric constant measurements revealed that a paraelectric-to-ferroelectric phase transition occurred at 122^{0}C and 123^{0}C for PS-BTO10 and PS-BTO25, respectively. By contrast, no phase transition was observed for PS-BTOc. It is noteworthy that for PS-BTO25 a transition at 10^{0}c suggested an additional tetragonal-to-orthorhombic phase transition. It was found that both phase and nanoparticle size of BaTiO$_3$ exerted a profound influence on the resulting dielectric properties of PS capped BaTiO$_3$ nanoparticles.

Experimental Procedure

PS-BTOc, PS-BTO10 and PS-BTO25 powders were hot-pressed into disk-shaped sample at 170^{0}C for 5 min. The specimens were cooled to room temperature and polished to ensure surface smoothness and then sputtered with a layer of silver on both sides served as electrodes. The dielectric spectra of these three samples were characterized by *Novocontrol* with the temperature and frequency ranging from -40^{0}C to 160^{0}C and 10^{-2}Hz to 10^6Hz, respectively at a temperature interval of 10^{0}C. The paraelectric-to-ferroelectric phase transition temperature was determined by measuring the dielectric constant of PS-BTO10 and PS-BTO25 samples at 1 kHz, 10 kHz, 100 kHz and 1 MHz in the vicinity of 130^{0}C at a 3^{0}C interval. Furthermore, the remnant polarization, P_r and coercive field, E_c were determined

from *P-E* hysteresis loops measured at room temperature using a standard ferroelectric test system (RT66A, Radiant Technologies).

Results and Discussion

Dielectric constants of PS-BTOc, PS-BTO10 and PS-BTO25

Figure 8 shows dielectric constants of PS-BTOc, PS-BTO10, and PS-BTO25 samples measured from -40^{0}C to 160^{0}C at four different frequencies (i.e., f = 1KHz, 10KHz, 100KHz, and 1MHz). The dielectric constant of tetragonal samples (i.e., PS-BTO10 and PS-BTO25) was much larger than that of cubic counterpart (i.e., PS-BTOc). More importantly, the temperature dependent dielectric constant curve of PS-BTOc indicated a relaxation behavior over a wide temperature range. An increase in dielectric constants around 130^{0}C was observed for the PS-BTO10 and PS-BTO25 samples, which can be attributed to a paraelectric-to-ferroelectric phase transition of BaTiO$_3$. To accurately determine the phase transition temperature, a scrutiny in the vicinity of 130^{0}C with a small temperature interval of 3^{0}C was conducted (**Figure 9**). Clearly, there existed a sharp peak at 122^{0}C and 123^{0}C for PS-BTO10 and PS-BTO25, respectively. We note that an apparent transition around 10^{0}C was observed for the PS-BTO25 sample (**Figure 8**). It is well known that, in addition to the cubic-to-tetragonal phase transition around 130^{0}C for BaTiO$_3$ bulk materials, there also exists a tetragonal-to-orthorhombic phase transition around 0^{0}C. Thus, the transition at 10^{0}C may be resulted from the tetragonal-to-orthorhombic phase transition of BaTiO$_3$. A detailed investigation in this regard is currently underway.
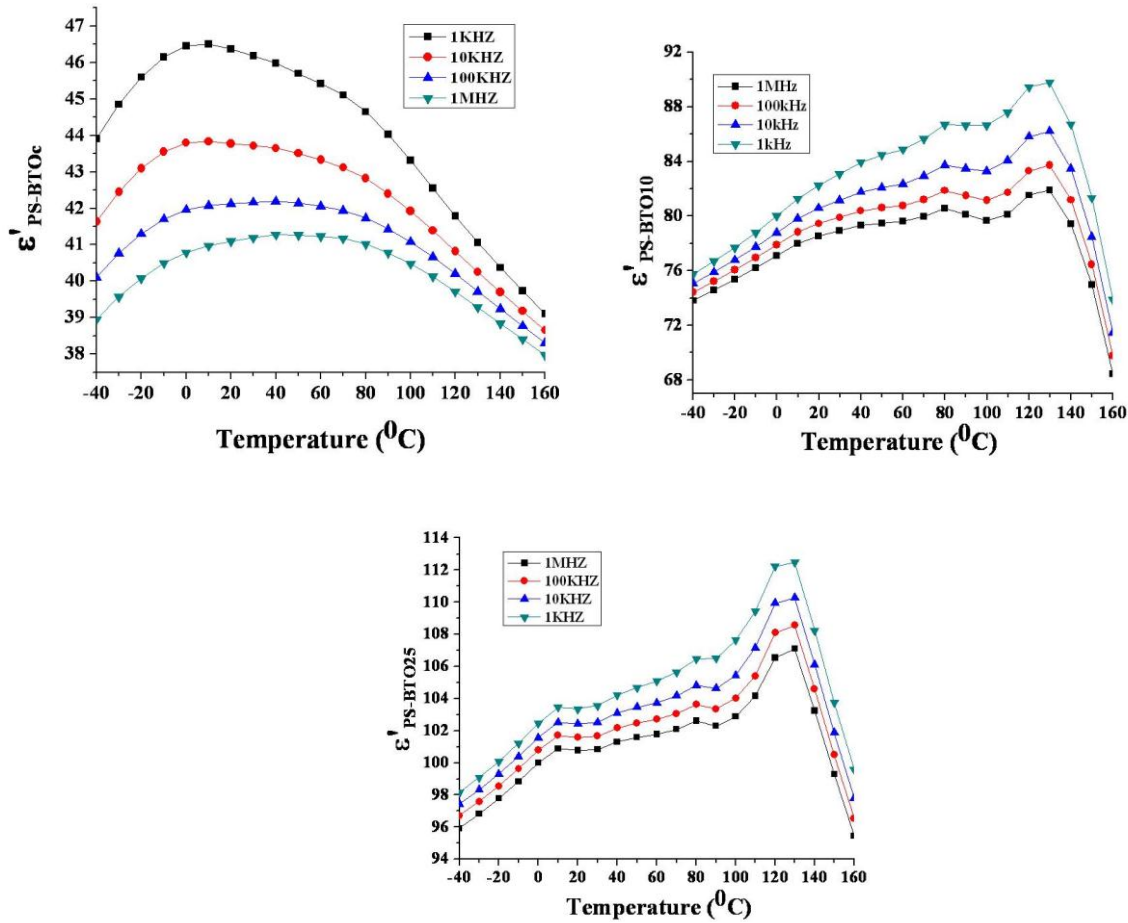

Figure 8. Dielectric constants of PS-BTOc (top left), PS-BTO10 (top right), and PS-BTO25 (bottom) samples measured from -40^{0}C to 160^{0}C at four different frequencies (i.e., f = 1KHz, 10KHz, 100KHz, and 1MHz).
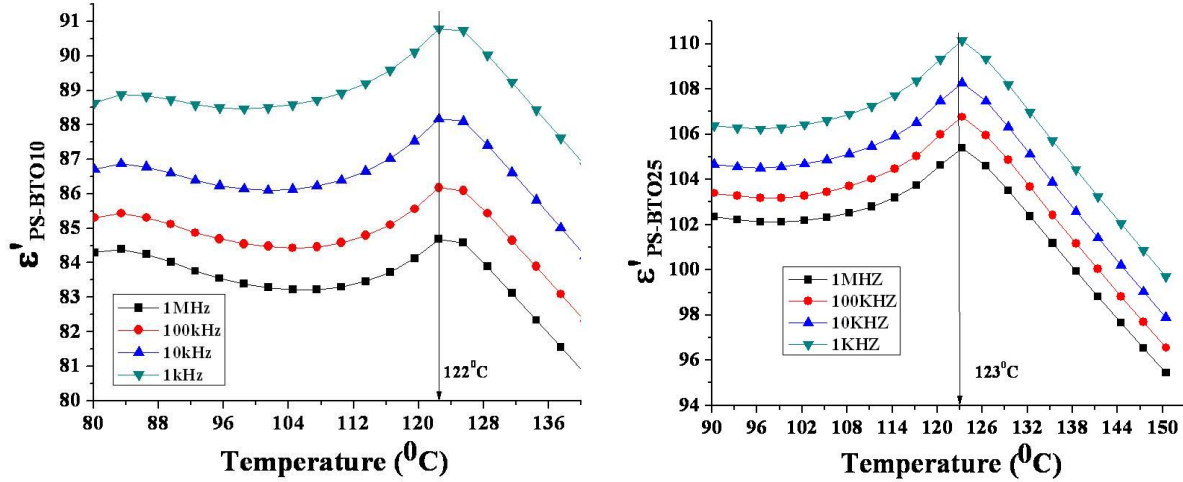
Figure 9. Paraelectric-to-ferroelectric phase transition of PS-BTO10 (left) and PS-BTO25 (right) nanoparticles, respectively.

Table 2. Volume fraction of PS in PS-BTO nanoparticles and the calculated density of PS-BTO sample.

Sample	V_{PS}/V_{PS-BTO}	ρ_{PS-BTO} (g/cm^3)
PS-BTO10	45.62	3.75269
PS-BTO25	48.71	3.59911

The volume fraction of PS in PS-BTO samples was determined by TGA (**Table 2**). The volume fraction of PS in PS-BTO25 was larger than that in PS-BTO10. The permittivity of PS was much lower than that of BaTiO$_3$. Taken together, the PS-BTO25 sample was expected to have lower dielectric constant than PS-BTO10. However, the experimental results showed the opposite trend, signifying that the difference in the permittivity of PS-BTO25 and PS-BTO10 may be due to the size effect of BaTiO$_3$ nanoparticles.

P-E loops of PS-BTO (tetragonal) samples

Figure 10 shows the *P-E* hysteresis loops of PS-BTO10 and PS-BTO25 samples measured at electric field of 20kV/cm to 45kV/cm at room temperature. The values of remanent polarization (P_r), coercive field (E_c), and maximum polarization (P_{max}) derived from *P-E* hysteresis loops are summarized in **Table 3**. A simultaneous increase of remanent polarization and maximum polarization with the increase of electric field was observed for both samples.
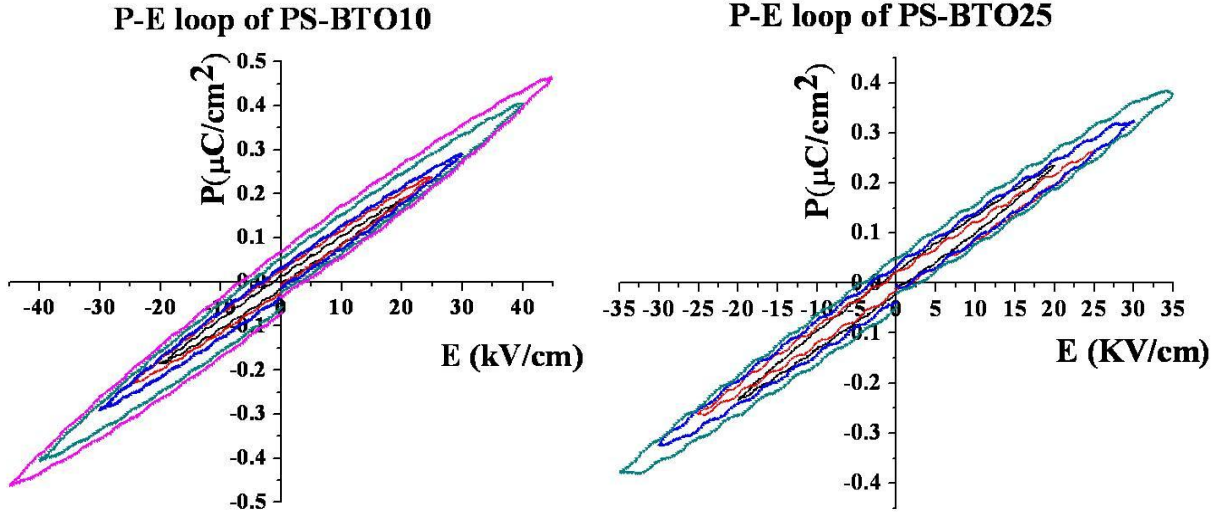
16

Figure 10. *P-E* loops of (a) PS-BTO25 and (b) PS-BTO10 nanoparticle samples.

Table 3. Remanent polarization (P_r), coercive field (E_c), and maximum polarization (P_{max}) of (a) PS-BTO25 and (b) PS-BTO10 measured at different electric fields.

(a)

E (kV/cm)	P_r (μC/cm^2)	E_c (kV/cm)	P_{max} (μC/cm^2)
20	0.02	1.17	0.23
25	0.02	2.17	0.26
30	0.03	1.90	0.32
35	0.05	2.80	0.38

(b)

E (kV/cm)	P_r (μC/cm^2)	E_c (kV/cm)	P_{max} (μC/cm^2)
20	0.01	0.56	0.19
25	0.02	1.48	0.24
30	0.03	2.18	0.29
40	0.05	4.36	0.40
45	0.07	5.63	0.46

4. Structure evolution and dielectric behavior of polystyrene-capped barium titanate nanoparticles

Polystyrene-capped barium titanate (BaTiO$_3$) nanoparticles with sizes of 11 nm and 27 nm were prepared using amphiphilic star-like diblock copolymer templates. The crystal structure evolution of these nanoparticles over a wide temperature range (10-428 K) was investigated by powder X-ray diffraction. The Rietveld refinement indicates that the abrupt structural transitions observed in micron-sized powders become broad as particle size is reduced to a few tens of nanometers. The orthorhombic phase (*Amm2*) is observed in the range of 10-388 K, coexisting with the rhombohedral phase (*R3c*) at lower temperatures and with the tetragonal phase (*P4mm*) at higher temperatures. At room temperature (300 K), polystyrene-capped BaTiO$_3$ nanoparticles, both 11 and 27 nm sizes, primarily adopt the tetragonal phase, transforming to the cubic phase ($Pm\overline{3}m$) at 398 K during heating. The phase evolution of the nanoparticles correlates well with their dielectric behavior. With the Landauer-Bruggeman effective approximation, the dielectric properties at room temperature for the BaTiO$_3$ core were calculated and the results are in agreement with the size effect of BaTiO$_3$ nanocrystals.

Introduction

Barium titanate (BaTiO$_3$), one of the most commonly used perovskite compounds for electrical devices, has been extensively studied with focus on its crystallographic transitions and dielectric/ferroelectric behaviors. A bulk BaTiO$_3$ crystal is in the paraelectric cubic phase with the $Pm\overline{3}m$ symmetry above the Curie temperature (T_C) of 403 K and becomes ferroelectric through a sharp displacive phase transition to the tetragonal P*4mm* phase. The ferroelectric BaTiO$_3$ crystal undergoes two further structural transitions to orthorhombic A*mm2* at 273 K (T_{OT}) and rhombohedral R*3m* at 183 K (T_{RO}).

A long-standing issue of interest concerning BaTiO$_3$ and other ferroelectric crystals is the so-called 'size effect', i.e. the size-dependence of their dielectric/ferroelectric properties and structural transitions. This issue is now particularly prominent and technologically relevant because the length scale of these crystals is in the nanometer range when they are applied in miniaturized electronic devices. Many theoretical and experimental studies have been conducted on BaTiO$_3$ in order to identify the critical size below which BaTiO$_3$ retains cubic paraelectric structure at room temperature, yet there is still no consensus on this issue. Based on X-ray diffraction experiments at several temperatures, Uchino *et al.* reported a critical size of 120 nm at which the T_C gradually lowered, and the cubic paraelectric phase became stable at room temperature. Aoyagi *et al.* reported similar findings with the critical size of approximately 100 nm. However, these results are not in agreement with other reports where the critical size was estimated to be on the order of 10-20 nm. Using the phenomenological Landau-Devonshire theory, Wang *et al.* calculated the critical size to be 44 nm. This value is close to the experimental results of Hoshina and Wada *et al.*, where a critical size of 30 nm was found. However, the T_C remains constant at 408 K for larger particles and the expected lowering of T_C when the particle size approaches 30 nm was not observed.

The particle size not only influences the Curie temperature, T_C, at which the paraelectric cubic and ferroelectric tetragonal transition occurs, but also impacts the ferroelectric transitions at T_{OT} and T_{RO}. Again, the reports in the literature are inconsistent. An X-ray diffraction study indicates that T_{OT} shifts from 285 K down to 260~270 K when the particle size decreases to 100 nm while a low-temperature heat-capacity measurement on 100 nm particles shows that T_{RO} does not display any anomaly. However, these observations seem to contradict a differential scanning calorimetry investigation where an increase of T_{OT} was noticed with decreasing grain size. Hoshina and Wada *et al.* found that, for BaTiO$_3$ particles larger than the critical size 30 nm, T_{OT} was independent of particle size while T_{RO} moves to higher temperatures with decreasing particle size. In contrast, several studies suggested an increase in T_{RO} and T_{OT}, and a decrease in T_C with the decreasing crystal size.

Most previous studies on the size effect in $BaTiO_3$ were focused on nominally bare particles, polycrystalline ceramics or even $BaTiO_3$/polymer composites. Polymer-capped $BaTiO_3$ nanoparticles have rarely been synthesized and characterized. In the present work, two sizes of polystyrene-capped $BaTiO_3$ (PS-BTO) nanoparticles, with $BaTiO_3$ core of 11 nm (PS-BTO11) and 27 nm (PS-BTO27) diameter were synthesized by chemical routes and their structure evolution was examined by powder X-ray diffraction. With the PS capping, the nanoparticles were hot-pressed into fully dense nanocomposite specimens (without growth of the original $BaTiO_3$ core) and their dielectric behaviors were evaluated.

Experimental

Synthesis. First, four amphiphilic 21-arm, star-like poly(acrylic acid)-b-polystyrene (PAA-*b*-PS) diblock copolymers with precisely tailorable molecular architectures, different molecular weight, and varied PAA to PS block ratios were synthesized by sequential atom transfer radical polymerization according to a previously described procedure. Ferroelectric $BaTiO_3$ nanoparticles were then synthesized via a wet chemistry approach by interacting nanoparticle precursors with the inner PAA block of star-like PAA-*b*-PS diblock copolymer. In a typical process, a certain amount of star-like PAA-*b*-PS (the molecular weights of each PAA and PS arm are 8.4k, and 5.2k, respectively) template was dissolved in N,N-Dimethylformamide (DMF) at room temperature to form unimolecular micelles, followed by the addition of the appropriate amount of precursors (i.e., $BaCl_2 \cdot 2H_2O + TiCl_4 + NaOH$) that can be selectively incorporated into the inner PAA core through the coordination bonding between the acetic acid group in PAA block and the metal ions of precursors. These $BaTiO_3$ precursors are not expected to interact with the outer PS shell as the PS block does not have any active functional groups to coordinate with the precursors. The solution was then refluxed at 180 ^{o}C under argon for 2 hours, yielding ferroelectric $BaTiO_3$ nanoparticles (diameter = 11 nm) capped with hydrophobic PS. PS capped $BaTiO_3$ nanoparticles with diameter 27 nm were also prepared by using star-like PAA-*b*-PS diblock copolymers of a different molecular weight and ratio of two dissimilar blocks (i.e., PS and PAA) as a template. The size and morphology of PS-capped $BaTiO_3$ nanoparticles were characterized by transmission electron microscopy (JEOL 1200EX STEM). The volume fraction of $BaTiO_3$ nanoparticles in the PS-BTO nanocomposites was determined by thermogravimetric analysis (TGA).

For comparison, micron-sized $BaTiO_3$ powder was also prepared via the solid-state reaction approach by reacting stoichiometric amounts of TiO_2 (purity 99.99 wt.%) and $BaCO_3$ (purity 99.9 wt.%) at 1373 K for 6 h.

Low temperature powder X-ray diffraction. The PS-BTO nanoparticles and micron-sized $BaTiO_3$ particles were mixed with GE varnish in a copper sample holder. After curing, the samples were polished using 400 grit sandpaper in order to produce the flat surface required for the Bragg-Brentano powder diffraction geometry. The isothermal X-ray powder diffraction measurements were carried out at different temperatures ranging between 320 and 5 K during cooling on a Rigaku TTRAX rotating anode powder diffractometer employing Mo Kα radiation. The diffractometer is equipped with a continuous flow ^{4}He cryostat controlling the sample temperature. The scattered intensity was recorded as a function of Bragg angle (2θ) using a scintillation detector with a step of 0.01^o 2θ. The maximum intensity to lowest background intensity ratio was close to 350 with the strongest Bragg peaks registering nearly 7000 counts at their peak values, which corresponds to ~1.2% statistical spread. The range of measured Bragg angles was from 8° to 56° 2θ. The program LHPM Rietica was employed to carry out the full-profile Rietveld refinement of every recorded pattern. The significant peak overlapping occurring due to crystallographic similarities of different polymorphic modifications of $BaTiO_3$ complicated the quantitative phase analysis of these phases, especially in the PS-BTO11 and PS-BTO27 samples. Several assumptions were made during the refinement, including (1) the atomic coordinates were fixed to be the same in the corresponding crystal structures for both micron-sized and nano-sized powders; (2) the profile parameters used in the Rietveld refinement were the same for all crystallographic polymorphs in the entire temperature range studied, for a given particle size; (3) the isotropic thermal displacement parameters of all atoms in each phase were assumed to be the same at a given temperature employing, in effect, the

overall isotropic thermal displacement approximation; (4) the rhombohedral angle of the low temperature structure of nano-sized samples was fixed to the value obtained during the refinement of the micron-sized powder. These assumptions did not, however, degrade the quality of the refinement as can be seen from the values of the profile residuals, $R_p \sim 0.09$, and the derived Bragg residuals, $R_{Bragg} \sim 0.02$ to ~ 0.04.

High temperature powder X-ray diffraction. The high temperature X-ray powder diffraction measurements were carried out on a PANalytical X'Pert PRO diffractometer equipped with a temperature controlled hot stage using Cu Kα radiation. The loose "as prepared" powders (not mixed with varnish or sintered) were used in this experiment. The diffraction data were collected at constant temperatures during heating, at 10 K intervals, from 298 K to 428 K. At each temperature, the scattered intensity was recorded as a function of Bragg angle (2θ) using an X'Celerator detector with a step size 0.0167° in the 2θ range from 10° to 120°. The collection time at each step was 120 s. Pure silica (hexagonal form) was used as an internal standard. The increase in the height of the sample stage arising from expansion of the alumina support rod was compensated for using a step motor. General Structural Analysis System (GSAS)[i] software was employed to carry out the full-profile Rietveld refinement of every recorded pattern. Scale factor, lattice parameters, background (6 order shifted Chebyshev polynomial approximation), and Pseudo-Voigt profile function (only Lorentzian crystalline broadening coefficient LX and Gaussian instrument response coefficient GW) parameters were refined initially. In the later stages of the refinements, atomic parameters of heavy elements Ti and Ba were also refined. The profile residuals, R_p, were less than 0.09, and the derived Bragg residuals, R_{Bragg}, were between ~0.04 to ~0.07.

Dielectric characterization. Disk-shaped samples for dielectric measurement, with diameter approximately 12.5 mm and thickness approximately 1 mm, were prepared using a hot press. PS-BTO powders were heated to 443 K and die-pressed at 21 MPa for 5 minutes. A thin film of silver was then sputtered on both flat surfaces as electrodes. Dielectric constant and loss tangent under the weak electric field were measured at 1, 10, 100 kHz with an LCZ meter (KEITHLEY 3330) in conjunction with a temperature chamber. Measurements below room temperature were carried out during continuous cooling with liquid N_2 to 113 K at a rate of 3 K/min while those above room temperature were performed during continuous heating to 433 K at the same rate. As a reference, dielectric measurements were also made on a pure PS sample with a Novocontrol dielectric spectrometer at constant temperatures during heating at 10 K intervals between 233 K and 403 K.

Results and Discussion

Transmission electron microscopy was used to examine the particle size and morphology of PS-BTO nanoparticles. As shown in Figure 1, all particles were nearly spherical in shape. According to image analysis, the particle sizes are 11 ± 1.2 nm and 27 ± 2.1 nm, respectively. The volume fractions of the inorganic $BaTiO_3$ core calculated from the mass loss from TGA tests are 45.6% and 48.7%, respectively.

The profiles of the pseudo-cubic $(111)_c$ and $(200)_c$ Bragg peaks of the PS-BTO nanoparticles at selected temperatures are displayed in **Figure 11**, with those from the micron-sized $BaTiO_3$ particles shown in Figure 1(e) as a reference. Except the profiles at 420 K indicating a single cubic phase, all other peak profiles in Figure 1 for both PS-BTO11 and PS-BTO27 have to be fitted with two or three Bragg peaks representing coexisting polymorphic phases of $BaTiO_3$. The Rietveld refinement at low temperatures was performed assuming a two-phase mixture, either orthorhombic-rhombohedral, or orthorhombic-tetragonal. There is a clear difference between the Bragg peak profiles of the PS-BTO nanoparticles and the micron-sized $BaTiO_3$. Presumably the PS capping on the nanoparticles does not contribute to the Bragg intensity, and the difference cannot be explained by strain-size broadening of the Bragg peaks alone. The X-ray diffraction patterns of micron-sized $BaTiO_3$ particles (only a small 2□ region is shown for clarity) indicate a single phase at each temperature shown in Figure 1(e), which is consistent with the typical phase transition sequence of conventional (not nanosized) $BaTiO_3$ materials. Both PS-BTO11 and PS-BTO27 nanoparticles display similar $(111)_c$ peak splitting but a more diffuse $(200)_c$ peak when compared with the micron-sized $BaTiO_3$ powder.
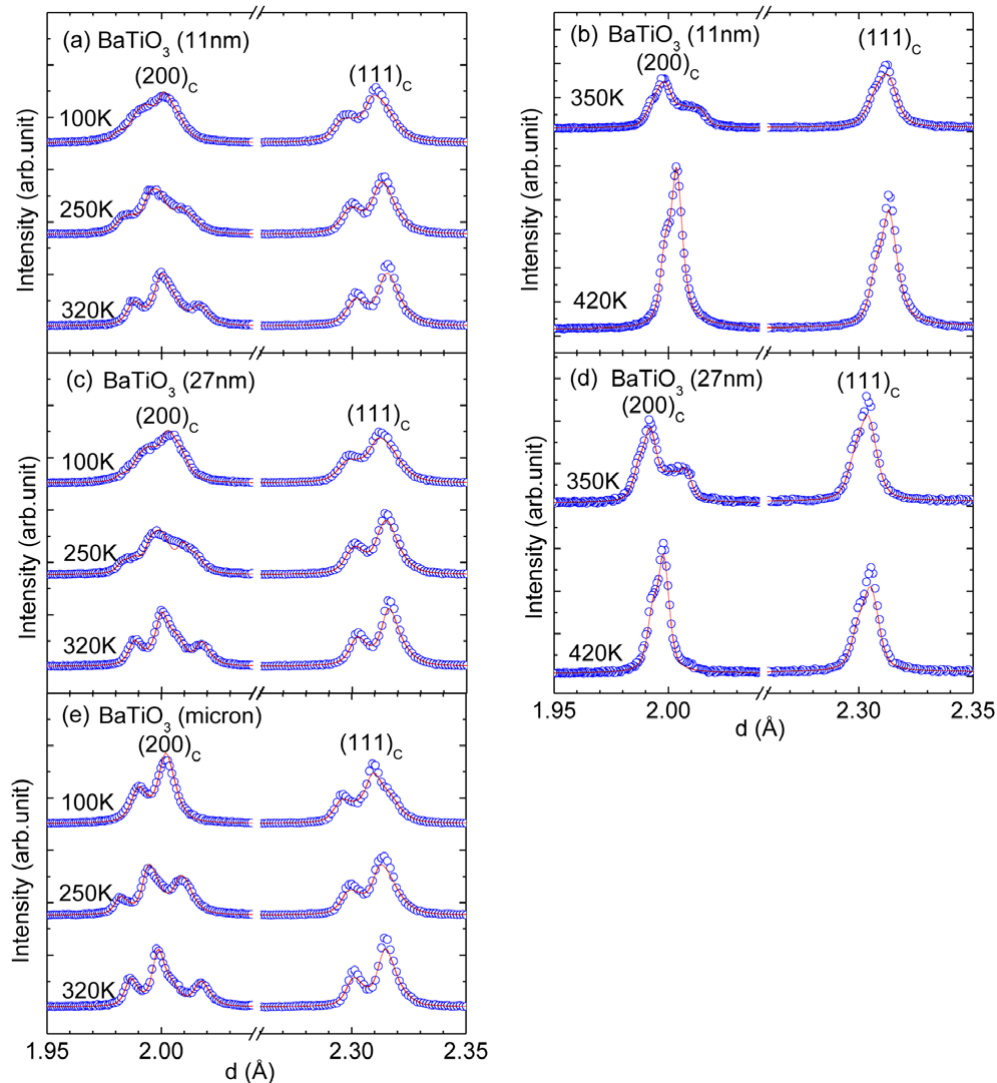
Figure 11. X-ray diffraction peak profiles at selected temperatures for the pseudo-cubic $(200)_c$ and $(111)_c$ from (a) PS-BTO11 at low temperatures, (b) PS-BTO11 at high temperatures, (c) PS-BTO27 at low temperatures, (d) PS-BTO27 at high temperatures, and (e) micron-sized $BaTiO_3$ powder at low temperatures.

The volume fraction of each phase as a function of temperature in PS-BTO11 and PS-BTO27, as well as that in the micron-sized $BaTiO_3$, is plotted in **Figure 12**. It is easy to notice a slight difference (~ 15 %) between phase compositions near room temperature determined by high-temperature vs. low-temperature X-ray diffraction methods. Such discrepancy can be explained by (a) different particle environment (loose powder vs. embedded in varnish); (b) the difference in the instrument resolution (resolution is higher for the low temperature data); and (c) the difference in absorption of X-rays by both the $BaTiO_3$ cores and polymer caps (low energy Cu K□ radiation is absorbed to a much greater degree compared with the high energy Mo K□ radiation). Nevertheless, there is a clear qualitative agreement between the high-temperature and low-temperature X-ray powder diffraction data indicative of a coexistence of tetragonal (main) and orthorhombic (minority) phases at room temperature in the nanoparticles.
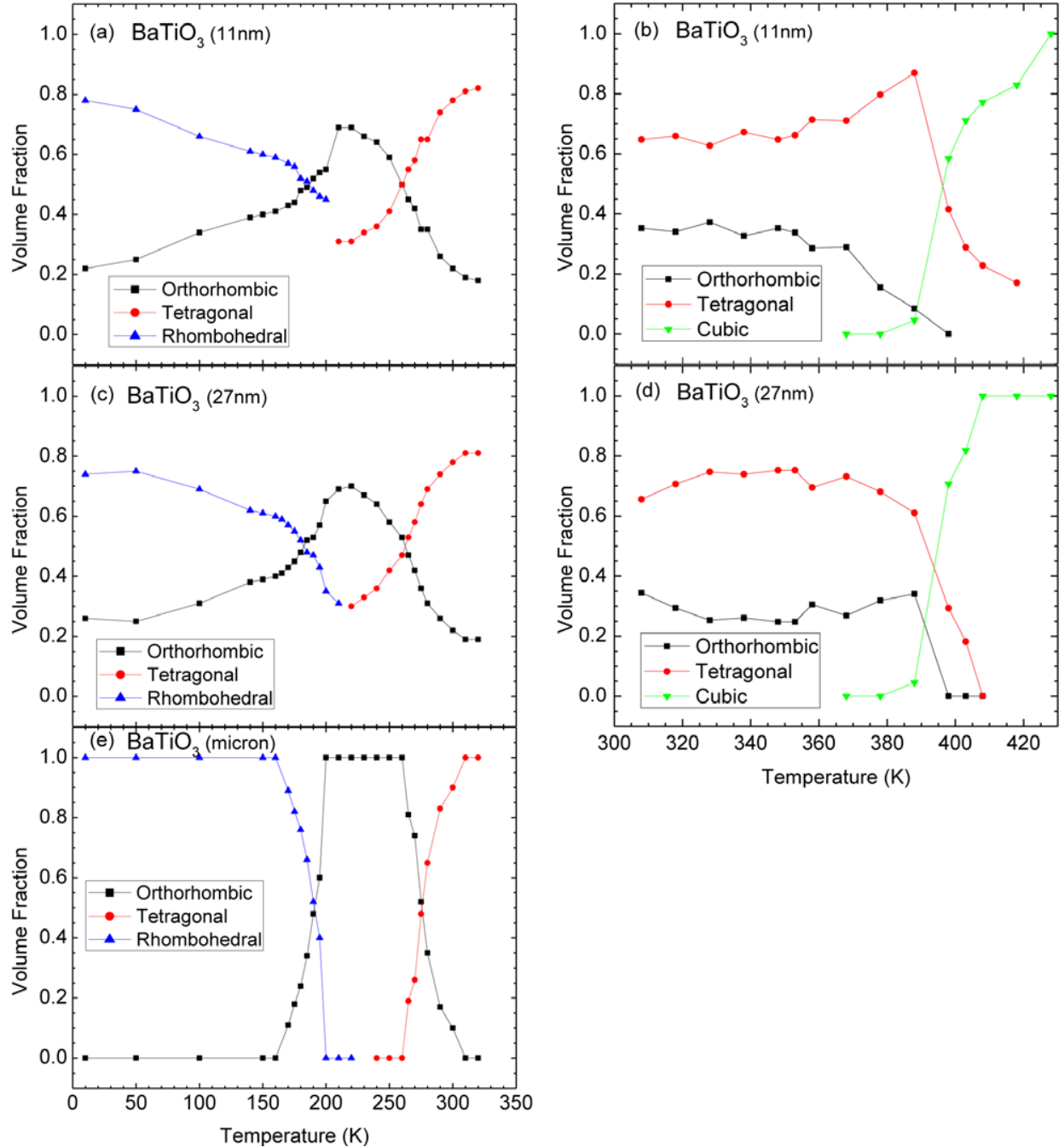
21

Figure 12. Temperature dependence of the volume fraction of the various phases in (a) PS-BTO11 at low temperatures, (b) PS-BTO11 at high temperatures, (c) PS-BTO27 at low temperatures, (d) PS-BTO27 at high temperatures, and (e) micron-sized BaTiO₃ powder at low temperatures.

The low-temperature experiment performed for the micron-sized BaTiO$_3$ powder shows two mixed-phase regions: the coexistence of rhombohedral and orthorhombic phases between 160 K and 200 K; orthorhombic and tetragonal phases between 260 K and 310 K. At other temperatures, single phases are observed. In the PS-BTO11 and PS-BTO27 nanoparticles containing ~80% of tetragonal phase and ~20% orthorhombic phase at room temperature, the tetragonal phase gradually transforms to the orthorhombic phase during cooling to low temperatures. The amount of the orthorhombic phase reaches a peak value of

~70% at ~210 K. Further decrease in temperature leads to a gradual formation of the rhombohedral phase, reaching the maximum ~80% at 10 K. During the warming-up of these PS-BTO nanoparticles from 308 K to 428 K, the volume fraction of the coexisting orthorhombic and tetragonal phases stays more or less the same up to 388 K. At 398 K, the orthorhombic phase disappears and both PS-BTO11 and PS-BTO27 become a mixture of the tetragonal and cubic phases with the cubic one dominant. The PS-BTO11 becomes single cubic phase at 428 K while the PS-BTO27 becomes single cubic phase at 408 K.

It is also noted that the level of the lattice distortion is directly related to the particle size. The lattice parameters of the major phase at different temperatures are listed in Table 4 for both PS-BTO11 and PS-BTO27, as well as the micron-sized BaTiO$_3$ powder. Using the tetragonal phase at 320 K as an example, the c/a ratio of the tetragonal lattice decreases from 1.0094 for the micron-sized powder to 1.0088 for PS-BTO27, and 1.0084 for PS-BTO11. For the orthorhombic lattice the b and c lattice parameters become closer in PS-BTO nanoparticles as compared to the micron-sized powder.

Table 4. Lattice parameters for the major phase of BaTiO$_3$ particles at selected temperatures.

Temperature (K)	Symmetry	BaTiO$_3$ (11 nm)	BaTiO$_3$ (27 nm)	BaTiO$_3$ (micron)
100	R$3m$	a = 4.0056(1)	a = 4.0063(1)	a = 4.0069(1)
		α = 89.87°	α = 89.87°	α = 89.86°
250	A$mm2$	a = 3.9915(1)	a = 3.9904(2)	a = 3.9910(1)
		b = 5.6888(4)	b = 5.6869(4)	b = 5.6798(2)
		c = 5.6777(3)	c = 5.6969(6)	c = 5.6914(3)
320	P$4mm$	a = 4.0014(1)	a = 4.0012(1)	a = 3.9998(1)
		c = 4.0350(1)	c = 4.0364(1)	c = 4.0373(1)
420	P$m\bar{3}m$	a = 4.0112(1)	a = 4.0113(1)	

It should be noted that although the two-phase coexistence, either orthorhombic-rhombohedral, or orthorhombic-tetragonal was assumed at low temperatures for the Rietveld refinement, it remains possible that three phases, i.e. orthorhombic, rhombohedral, and tetragonal may coexist in a limited temperature range around 210 K. This is similar to the coexistence of orthorhombic, tetragonal and cubic phases at temperatures around 400 K. However, this does not necessarily mean that all of the phases coexist in individual nanoparticles. It is also possible that each individual nanoparticle is single phase. Due to size and chemistry variation, some of them are in the orthorhombic phase while others are in the tetragonal phase at room temperature.

The temperature dependent dielectric properties of PS-BTO11 and PS-BTO27 were measured on hot-pressed dense nanocomposite disks. As shown in **Figure 13**, data below room temperature were taken during cooling while those above room temperature were recorded during heating in order to be consistent with the X-ray powder diffraction experiments. For the PS-BTO11, the dielectric constant shows a monotonic decrease during cooling from room temperature to 113 K. In this range, there is only one noticeable anomaly at ~283 K (Figure 3a) which may correspond to the fast increase of the orthorhombic phase volume fraction (T_{OT}). During heating of the PS-BTO11 sample, an obvious frequency dispersion in the dielectric properties is seen, and two peaks can be found at ~363 K and ~413 K on the dielectric constant curves (Figure 3b). The peak at ~413 K is apparently related to the abrupt formation of the cubic phase (T_C). The PS-BTO27 sample displays a higher dielectric constant with weaker frequency dispersion. In addition, the dielectric anomalies become more apparent during the cooling process; one at ~273 K on the dielectric constant curves and the other at ~210 K on the loss tangent curves (Figure 3c). Apparently, the anomaly at ~273 K is associated with the formation of the orthorhombic phase (T_{OT}) while the other one is related to the formation of the rhombohedral phase (T_{RO}). The dielectric anomalies also become more prominent during heating in PS-BTO27 than in PS-BTO11,
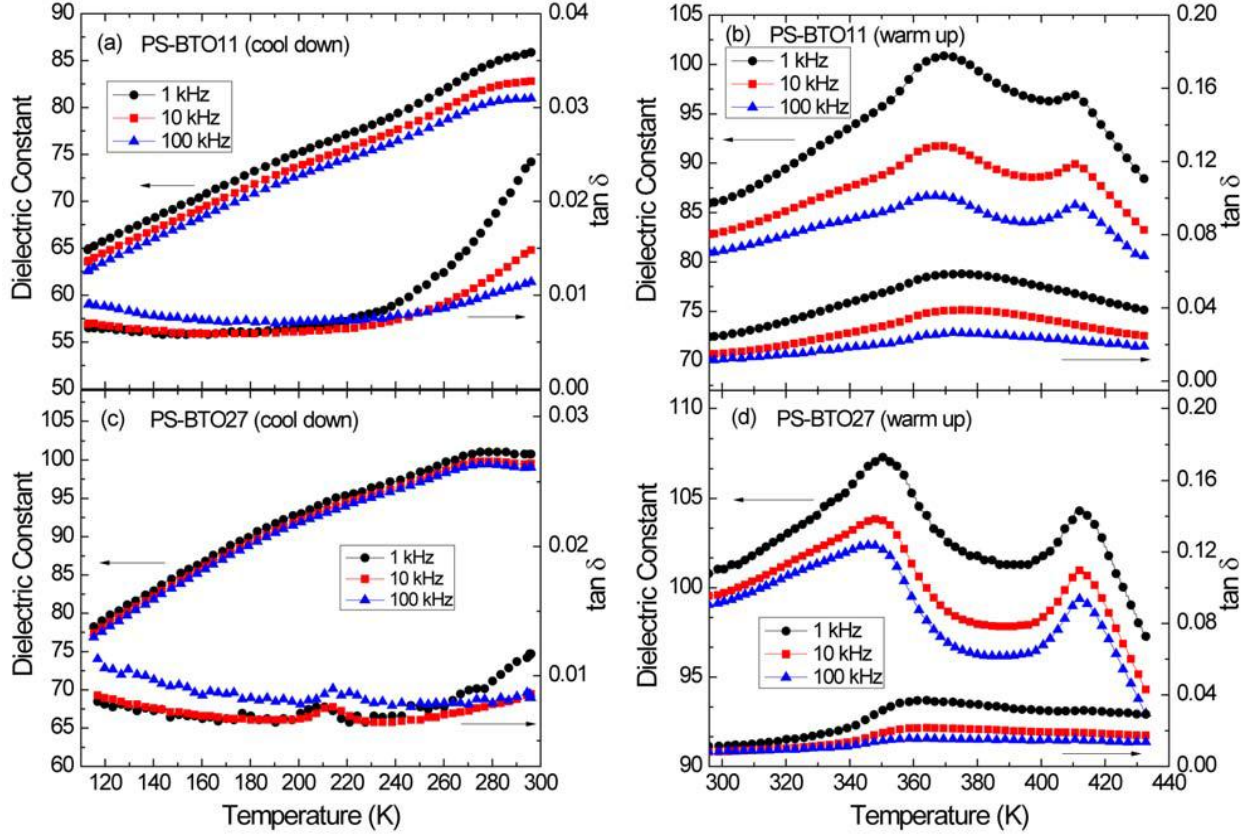
Figure 13. Temperature dependence of dielectric properties of (a) PS-BTO11 during cooling, (b) PS-BTO11 during heating, (c) PS-BTO27 during cooling, and (d) PS-BTO27 during heating.

with one at ~353 K and the other at ~413 K (Figure 3d). Again, the dielectric peak at ~413 K originates from the formation of the cubic paraelectric phase (T_C). Compared with the sharp transitions in conventional $BaTiO_3$ powders, transitions in PS-capped $BaTiO_3$ nanoparticles are broadened and smeared. Especially in PS-BTO11, the transition at T_{RO} becomes invisible and that at T_{OT} is hardly seen from dielectric measurements. This can be attributed to the size distribution of nanoparticles, the persistence of the orthorhombic phase throughout the temperature range due to an incomplete structural transition, and the dilution effect from non-ferroelectric PS. In addition, it appears that all transition temperatures, T_{RO}, T_{OT}, and T_C are shifted to higher temperatures in these PS-capped nanoparticles compared to micron sized $BaTiO_3$.

The dielectric anomalies at ~363 K in PS-BTO11 and at ~353 K in PS-BTO27 do not correspond to any structural changes in the $BaTiO_3$ core. Our differential scanning calorimetry measurements on pure PS with the same molecular weight as those capping the $BaTiO_3$ nanoparticles indicate that PS undergoes the glass transition in this temperature range. Furthermore, dielectric properties measured at discrete temperatures with 10 K intervals on pure PS, **Figure 14**, confirm the presence of a dielectric anomaly at the glass transition temperature.

The PS-BTO samples for dielectric measurements can be considered as a composite of two phases: PS as the matrix and the $BaTiO_3$ nanoparticles as the inclusion. Various models have been used for the evaluation of the dielectric constant of two phase composites. With these models, the effective dielectric constant of the $BaTiO_3$ core can be extracted from the data obtained from the dielectric measurements of PS-BTO nanocomposites. Considering the high volume fraction of the $BaTiO_3$ nanoparticles, the
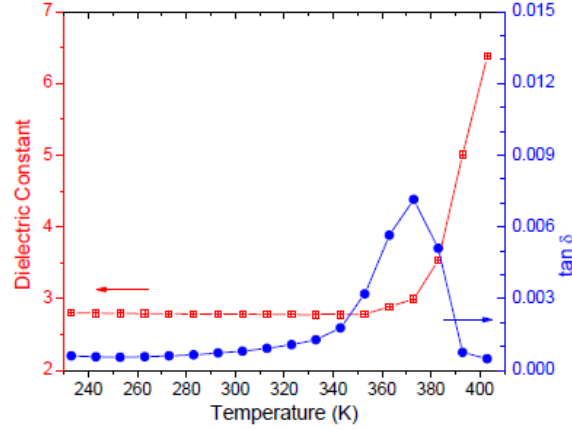
Figure 14. Temperature dependence of dielectric properties of pure PS measured at 1 kHz at constant temperatures with 10 K intervals during heating.

Landauer-Bruggeman effective approximation is appropriate for the calculation. The mathematical expression of the approximation is

$$\gamma \frac{\varepsilon_1 - \varepsilon_{eff}}{\varepsilon_1 + 2\varepsilon_{eff}} + (1 - \gamma) \frac{\varepsilon_2 - \varepsilon_{eff}}{\varepsilon_2 + 2\varepsilon_{eff}} = 0 \qquad (1)$$

where γ denotes the volume fraction of the inclusion, and ε_{eff}, ε_1 and ε_2 stand for the dielectric constant of the nanocomposite (PS-BTO), inclusion (BaTiO$_3$) and matrix (PS), respectively. In this study, the dielectric constant of PS at room temperature was measured to be between 2.76 and 2.80 in the frequency range of 1 Hz to 1 MHz (as can be seen in Figure 4, for 1 kHz). The measured effective dielectric constant of the PS-BTO nanocomposites and calculated dielectric constant of BaTiO$_3$ nanoparticles in this frequency range are shown in **Figure 15**. PS-BTO27 shows higher and more stable effective dielectric constant than PS-BTO11. Using Eq. (1), the dielectric constant of 27 nm BaTiO$_3$ nanoparticle (BTO27) decreases from 387 to 354 as the frequency increases from 1 Hz to 1 MHz, whereas that of 11 nm nanoparticles (BTO11) is in the range from 310 at 1 Hz to 235 when the frequency reaches 1 MHz. Combined with the X-ray diffraction structural analysis results, the dielectric data suggest that the critical size for PS-capped BaTiO$_3$ nanoparticles is below but close to 11 nm.
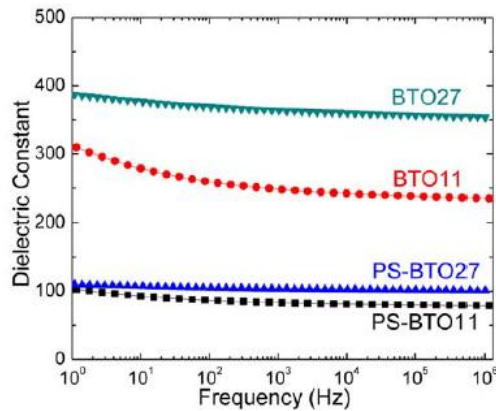

Figure 15. The frequency dependence of dielectric constant at room temperature of PS-BTO11 and PS-BTO27 and the calculated dielectric constant of the BaTiO$_3$ cores. BTO11 denotes the 11 nm core while BTO27 denotes the 27 nm core.

PS-capped $BaTiO_3$ (PS-BTO) particles with sizes of 11 nm and 27 nm were prepared by a novel chemical route. Structural analysis demonstrates that the tetragonal phase is the dominant phase while the orthorhombic phase is also present in these nanoparticles at room temperature. The phase transitions in PS-BTO nanoparticles occur over broad temperature ranges, and two phase coexistence is observed from 10 K to 428 K for PS-BTO11 and from 10 K to 408 K for PS-BTO27. As a consequence of the presence of multiple phases and the diluting polymer matrix, the anomalies of the dielectric properties associated with the structural phase transitions are broadened. With decreasing particle size, the $BaTiO_3$ shows less lattice distortion and lower dielectric constant at room temperature. These results indicate a critical size of less than 11 nm for these PS-capped $BaTiO_3$ nanoparticles.

5. Dielectric relaxations of PMMA and PS-*b*-PMMA diblock copolymers

The dielectric relaxation properties of one PMMA homopolymer and two PS-*b*-PMMA diblock copolymers (molecular weight: 50-50K and 50-130K) were investigated by broadband dielectric spectroscopy in a frequency range from 10^{-2} to 10^6 Hz and a temperature range from -40 ^{0}C to 150 ^{0}C. α relaxation associated with the glass transition, secondary β relaxation due to localized motions, and the conductivity at low frequency were identified and modeled for all samples via parameter fitting. Based on the modeling results, the characteristic relaxation time, fragility index, activation energy, and relaxation strength of PMMA and PS-*b*-PMMA were compared.

Dielectric spectroscopy technique has been proven as an effective way in monitoring dynamics of materials over a broad temperature and frequency range. Localized rotations of side chains or groups and cooperative motions of segments or backbone chains are main dielectric relaxation mechanisms of amorphous polymers. PS as a nonpolar polymer is not dielectrically active. For PMMA, there are two dielectric relaxation mechanisms, structural α type relaxation and localized β type relaxation; α-relaxation arises from the backbone motion in the form of glass transition of polymer while β-relaxation accounts for the localized rotational fluctuations of dipole vector.

To explore relaxation mechanisms of PMMA and PS-*b*-PMMA, the parameters describing their relaxation processes were fitted according to the Havriliak-Negami model[1] via the least-squares fitting technique.[2,3] Subsequently, the comparison between PS-*b*-PMMA and PMMA was performed in term of the fragility index, activation energy, characteristic relaxation time, and relaxation strength. The study of dielectric relaxations of homopolymer and copolymer aims to explore relaxation dynamics which depend on not only the morphology but also the degree of polymerization of polymer.

Results and Discussion

The molecular weights of samples used in the study are summarized in **Table 5**. The dielectric measurements were conducted using the broadband NOVOCONTROL spectroscopy.

Table 5. Molecular weights of PMMA and PS-*b*-PMMA diblock copolymers

	PMMA	PS-*b*-PMMA	PS-*b*-PMMA
Molecular weight	50K	50K-50K	50K-130K

The isochronal plots of PMMA, PS-b-PMMA diblock copolymers, and PS/PMMA blend at 25 Hz are shown in **Figure 16**. β relaxation, α relaxation, and conductivity occurred sequentially as the temperature increased. PMMA, PS-*b*-PMMA, and PS/PMMA showed a similar β relaxation peak as the β relaxation of PMMA dominated in this temperature range. As temperature increased, α relaxation peak, associated with the glass transition temperature T_g, was visible for all samples. However, α relaxation

peak of PS-*b*-PMMA was almost undetectable and difficult to be separated from the conductivity effect at higher temperature.
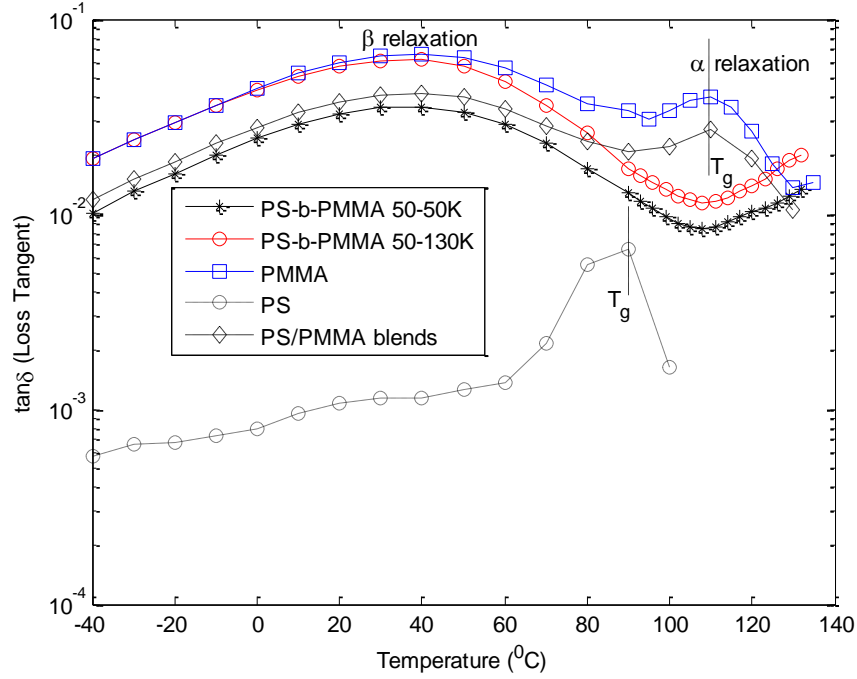

Figure 16. Isochronal plots of PS, PMMA, PS/PMMA blend, and PS-*b*-PMMA diblock copolymers at 25 Hz, in which different types of dielectric relaxations and glass transition temperatures were noted.

In order to further analyze the relaxation mechanisms, isothermal analysis was performed over a broad frequency range from 10^{-2} Hz to 10^{6} Hz. α, β relaxation processes and conductivity terms were modeled separately by the least-square fitting techniques.[2,3] The experimental data of dielectric spectra can be expressed as the sum of α and β relaxations and the conductivity term.

$$\varepsilon^*(\omega) - \varepsilon_\infty = \frac{\Delta\varepsilon}{[1 + (i\omega\tau_{HN})^{1-\propto_{HN}}]^{\beta_{HN}}} - \frac{i\sigma}{\varepsilon_0\omega^A}$$

where $\Delta\varepsilon$ is the dielectric strength, ε_∞ is the permittivity at infinite frequency, σ is the conductivity term, ε_0 is the vacuum permittivity, τ_{HN}, α_{HN} and β_{HN} are characteristic relaxation time and shape parameters that describe the Havriliak-Negami function.

A typical isothermal plots of PS-*b*-PMMA diblock copolymers (50-50K and 50-130K) at 105 ^{0}C are shown in **Figure 17**, where α, β relaxation processes and conductivity terms were identified. The superposition of α, β relaxations and the conductivity term agreed well with the experimental results.
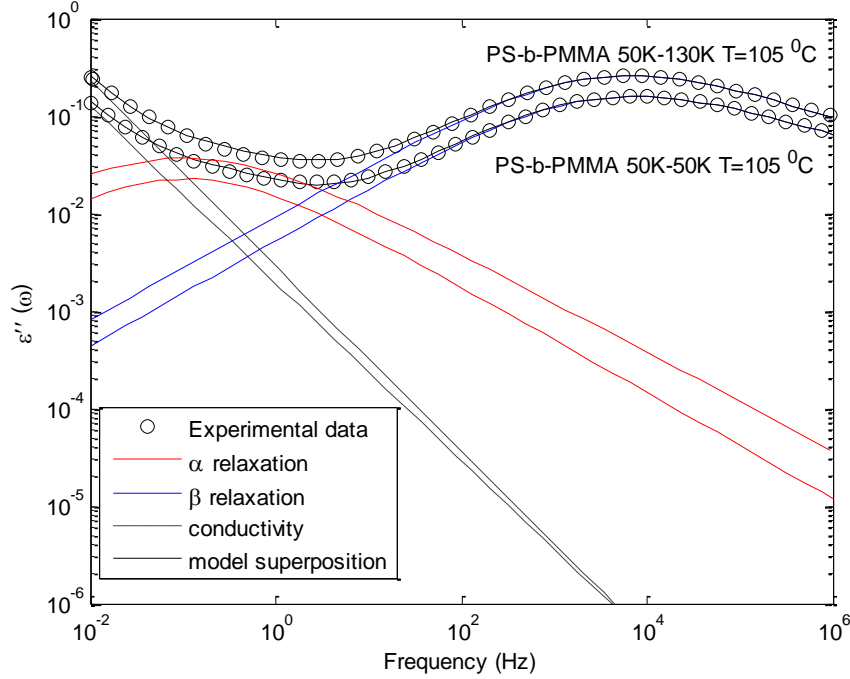
Figure 17. Isothermal plots of imaginary part of permittivity of PS-*b*-PMMA diblock copolymers at 105^{0}C.

For amorphous polymer PMMA, dielectric β relaxation process was originated from localized rotational fluctuations of side chains. The mechanisms of β relaxation were discussed by Goldstein and Johari,[13,14] who concluded that β relaxation universally exited in a great variety of amorphous polymers. The temperature dependence of characteristic relaxation time of β relaxation can be described by the Arrhenius law

$$f_{\beta,max} = f_0 \exp\left[-\frac{E_A}{k_B T}\right]$$

At glass transition temperature T_g, the glass state was transformed to a rubbery state. As temperature continued to increase, the rubbery state was transitioned to the terminal liquid state. Both segmental motions and chain connectivity of polymers contributed to the dynamic glass transition by intramolecular and intermolecular cooperativity. The characteristic relaxation rate of α relaxation which describes the viscosity and structural relaxation, followed Vogel-Fucher-Tammann law.[4-6]

$$f_{\alpha,max} = f_0 \exp\left[-\frac{DT_0}{T - T_0}\right]$$

where exponential factor f_0 is on the order of vibrational frequency, T_0 is the Vogel temperature, and D is the strength parameter. The fragility of polymers is related to the curvature of $f_{max} \sim 1/T$ plot, which is given as

$$m = \frac{d\log < \frac{1}{2\pi f_{max}} >}{dT_g/T_0}\Big|_{T=T_g}.$$

where *m* is the fragility index of polymers. After expressing in terms of VFT parameters, the fragility index *m* can be described by the following equation,

$$m = \frac{T_g}{\log 10} \frac{DT_0}{(T_g - T_0)^2}$$

The relation between the maximum relaxation time and the corresponding Havrilliak-Negami parameters is given as

$$f_{max} = f_{HN} \left\{ \frac{\sin\left[\frac{\pi\delta\gamma}{2(\gamma+1)}\right]}{\sin\left[\frac{\pi\delta}{2(\gamma+1)}\right]} \right\}^{-1/\delta},$$

The temperature dependent parameters for α and β relaxations of one PMMA and two PS-*b*-PMMA in the present study are shown in **Table 6**. The values of f_0 and f_{max} for copolymers were much smaller than that of PMMA, indicating the suppression of α relaxation in diblock copolymers as compared to PMMA. The fragility index of PS-*b*-PMMA (50K-50K) was similar to that of PMMA 50K as the fragile index of PS and PMMA was identical. However, the fragility index of PS-*b*-PMMA (50K-50K) was smaller than that of PS-*b*-MMA (50K-130K) because the fragility of PMMA generally increased with the molecular weight.

Table 6. Parameters of α and β relaxation processes of one PMMA and two PS-*b*-PMMA in the present study.

α relaxation	f_{max}	D	T_0 (K)	T_g (K)	m
PMMA	3.97e8	2.50	337	95.4	131
PS-*b*-PMMA (50K-50K)	4.21e2	0.56	354	96.8	126
PS-*b*-PMMA (50K-130K)	2.65e2	0.44	358	97.6	150

β relaxation	E_A (KJ, $T > T_g$)	E_A (KJ, $T < T_g$)
PMMA	78.7	98.7
PS-*b*-PMMA (50K-50K)	75.9	87.4
PS-*b*-PMMA (50K-130K)	82.7	83.0

α and β relaxations of PMMA and PS-*b*-PMMA plotted as a function of reciprocal temperature are shown in **Figure 18**. For β relaxation, all samples exhibited similar activation energies as the dominant β relaxation process was resulted from localized rotational motions of side chains of PMMA.
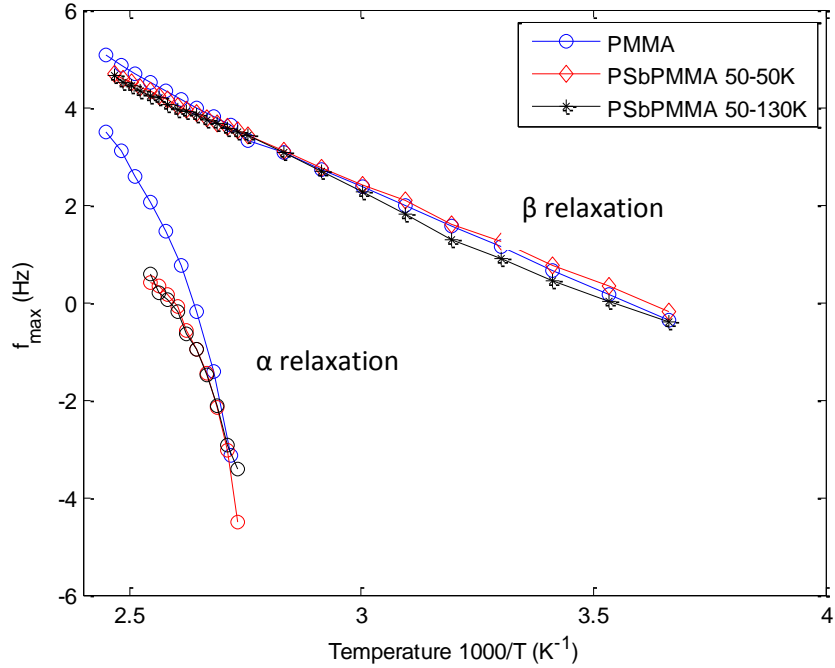
Figure 18. α and β relaxations of PMMA and PS-*b*-PMMA as a function of reciprocal temperature. f_{max} is the maximum frequency in the curve of ε"(f) ~ frequency.

At the end of low frequency and high temperature of a spectrum, both ε' and ε" exhibited unreasonably high values, which were not due solely to dielectric properties of samples, but also resulting from the electrode polarization effect due to space charge built up at the interface between the sample and the electrodes. To elucidate this DC and AC conductivity effect, the dielectric spectrum was converted into a conductivity spectrum according to the relation $\sigma^* = i\omega\varepsilon_0\varepsilon^*$. It was proposed by Johscher[7] that the conductivity can be expressed as the sum of DC and AC conductivity terms, and AC conductivity follows a power law dependence of frequency,

$$\sigma(\omega) = \sigma_{DC} + Z\omega^A$$

Where $0<A<1$ and σ_{DC} is the DC conductivity term. As shown in **Figure 19**, when the temperature was high enough, the conductivity was reduced to a plateau value, which can generally be regarded as accurate value of DC conductivity.
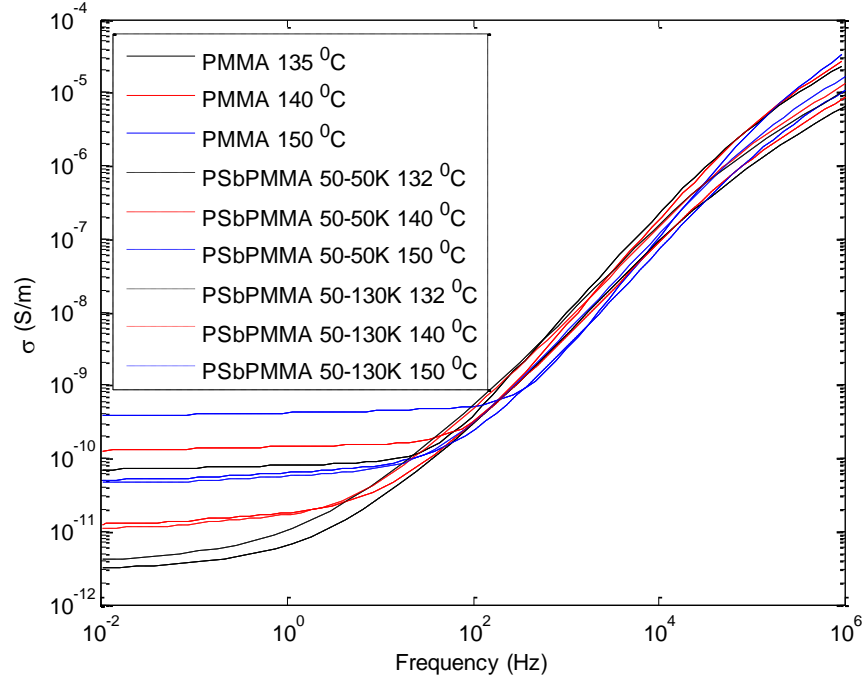
Figure 19. The real parts of conductivity of samples are plotted as a function of frequency at high temperatures.

The DC conductivity follows the Vogel-Fulcher-Tamman law[4-6]

$$\sigma_{DC} = \sigma_0 \exp\left[-\frac{A}{T - T_0}\right],$$

indicating that the transport mechanism of charge carriers of polymers was associated with the motions of polymer chains. The corresponding fitting parameters of DC conductivity terms are summarized in **Table 7**. Then, the conductivity term consisting of DC and AC conductivity can be extracted from dielectric spectrum and separated from relaxation processes, from which the accuracy of fitting procedures can be improved by reducing the effects of electrode polarization.

Table 7. Fitting parameters of VFT law that describe DC conductivity terms of PMMA and PS-*b*-PMMA.

DC conductivity	σ_0	A	T_0 (K)
PMMA	5.39e-4	1985	283
PS-*b*-PMMA (50K-50K)	5.15e-6	1075	330
PS-*b*-PMMA (50K-130K)	1.99e-1	3584	257

The dielectric strength of α and β relaxations can be predicted according to the Onsager/Kirkwood/Fröhlich theory,[8-12]

$$\Delta\varepsilon \sim F_{Onsager} g \frac{\mu^2 N_p}{k_B T V}$$

where $F_{Onsager} \approx 1$ is Onsager factor, N_p/V is the number of dipoles, μ^2 is the square of permanent dipole moment, g is the Kirkwood/Frohlich correlation factor describing the interaction between dipoles with respect to ideal dipoles,

$$g = 1 + \frac{< \sum_i \sum_{i<j} \mu_i \mu_j >}{N \mu^2} \approx 1 + z < \cos(\Psi) >$$

where z is the coordination number and Ψ is the angle between the dipole under test and the neighbor dipole.

For β relaxation, the number of dipoles per unit volume N_p/V increased with the temperature. However, the temperature dependent factor g was not significant as β relaxation can take place at low temperature where reorientation of dipole vectors can hardly occur. Therefore, the overall dielectric strength of β relaxation strength increased with temperature. Dielectric α relaxation associated with dynamic glass transition occurred above T_g. The contribution of cross-correlation term to the μ^2 term increased significantly when temperature decreased and approached T_g. Therefore, the dielectric strength of α relaxation decreased when the temperature increased.

The dielectric strengths of α and β relaxations of PMMA and PS-*b*-PMMA as a function of temperature are shown in **Figure 20**. The overall dielectric strengths $\Delta\varepsilon_\alpha$ of PS-*b*-PMMA for 50K-50K and 50K-130K were similar yet much smaller than that of PMMA. This is because α relaxation of PS-*b*-PMMA was suppressed by the morphology and configuration of copolymers. Because PS was not dielectrically active, β relaxation of all samples was due primarily to the localized rotational fluctuations of side chains or groups, and depended on the total number of dipoles which were influenced by the molecular weight of PMMA. The molecular weight of PMMA for PMMA and PS-*b*-PMMA (50K-50K) was same. However, the overall dielectric strength of PS-*b*-PMMA (50K-50K) due to the introduction a second phase PS to copolymers and the reduced values can be predicted by classic rule of mixture. As suggested by Onsager/Kirkwood/Fröhlich theory, the values of dielectric strength $\Delta\varepsilon_\beta$ of PS-*b*-PMMA (50K-130K) was larger than that of PS-*b*-PMMA (50K-50K) due to relatively larger molecular weight of PMMA in PS-*b*-PMMA (50K-130K).
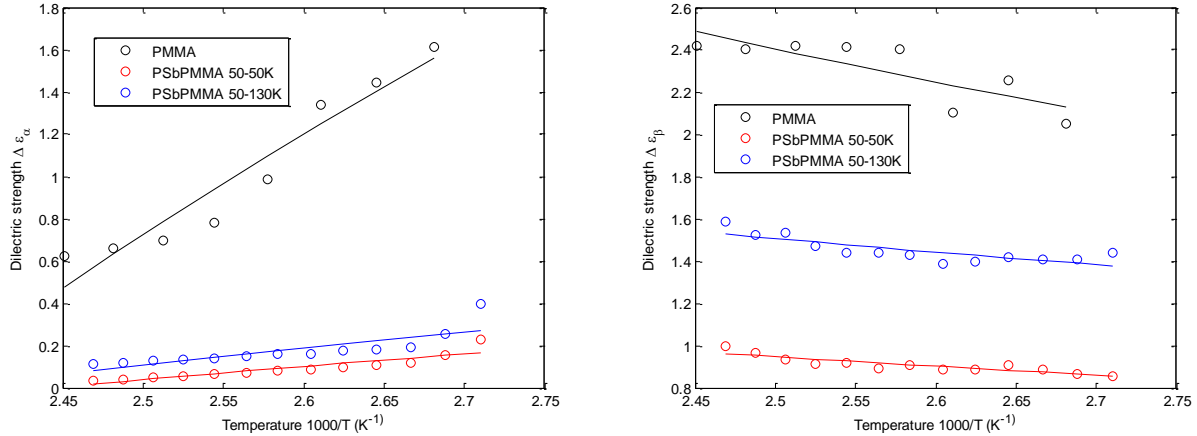

Figure 20. Dielectric relaxation strengths of α, β relaxations as a function of temperature for PMMA, PS-*b*-PMMA (50K-50K), and PS-*b*-PMMA (50K-130K).

References
1. S. Havriliak, S. Negami, *Polymer,* 1967, **8**, 161.
2. E. Schlosser and A. Schönhals, *Colloid Polym.Sci.*, 1989, **267**, 963.
3. J. Turnhout, M. Wübbenhorst, *dielectric newsletter,* November 2000, NOVOCONTROL GmbH,

Hundsangen.

4. V. Vogel, *Z. Phys.,* 1921, **22**, 645.

5. G. S. Fulcher, *J. Am. Ceram. Soc.,* 1925, **8**, 339.

6. G. Tammann and W. Z. Hesse, *Anorg. Allgem. Chem.*, 1926, **156**, 245.

7. A. K. Jonscher, *Nature* 1977, **267**, 673.

8. Onsager L*, J. Am. Chem. Soc.*, 1938, **58**, 1486.

9. J. G. Kirkwood*, J. Chem. Phys.*, 1939, **58**, 911.

10. J. G. Kirkwood, *Ann. NY Acad. Sci.,* 1940, **40**, 315.

11. J. G. Kirkwood, *Trans. Faraday Soc.,* 1946, **42A**, 7.

12. H. Fröhlich*, Theory of dielectrics*. Oxford University Press, London, 1958.

13. G. P. Johari, M. J. Goldstein*, J. Chem. Phys.,* 1980, **53**, 2372.

14. G. P. Johari, *J. Chem. Phys.,* 1973, **28**, 1766.

Publications

1. S.W. Hong, J. Wang, Z. Lin, "Evolution of ordered block copolymer serpentines into a macroscopic, hierarchically ordered web". *Angewandte Chemie International Edition* **48**, 8356 (2009).

2. J. Wang, X. Pang, M. Aknic, and Z. Lin, "Synthesis and Characterization of Perovskite PbTiO$_3$ nanoparticles with solution processibility", *Journal of Materials Chemistry* **20**, 5945 (2010)

3. X. Pang, L. Zhao, M. Akinc, J. K. Kim, and Z. Lin, "Novel amphiphilic multi-arm, star-like block copolymers as unimolecular micelles", *Macromolecules* **44**, 3746 (2011).

4. X. Pang, L. Zhao, C. Feng, and Z. Lin, "Novel amphiphilic multi-arm, star-kike coil-rod diblock copolymers via a combination of click chemistry with living polymerization", *Macromolecules*, **44**, 7176 (2011).

5. X. Pang and Z. Lin, "A general and robust strategy for monodisperse nanocrystals", *Nature Materials* (under review).

6. H. Guo, X. Pang, J. Liu, M. Akinc, N. Bowler, Z. Lin, and X. Tan, "Structure evolution and dielectric behavior of polystyrene-capped barium titanate nanoparticles", *Chemistry of Materials* (under review).

7. J. Liu, H. Guo, X. Pang, X. Tan, M. Akinc, Z. Lin, and N. Bowler, "Dynamics of polystyrene-b-poly(methylmethacrylate) (PS-b-PMMA) diblock copolymers and PS/PMMA blends: a dielectric study", *Journal of Non-crystalline Solids* (under review).

Patent

1. Z. Lin and X. Pang, "An extremely simple yet robust route to functional (and multifunctional) monodisperse nanoparticles, nanorods and nanotubes for use in energy and biomedical applications*"* (submitted to ISU Research Foundation on March 12, 2011; the utility patent was filed in June 2011)